論文 / 著書情報
Article / Book Information

題目(和文)	動的交通混雑のシステム特性
Title(English)	Systemic Properties of Dynamical Traffic Congestion
著者(和文)	加地大
Author(English)	Masaru Kaji
出典(和文)	学位:博士(工学), 学位授与機関:東京工業大学, 報告番号:甲第10924号, 授与年月日:2018年6月30日, 学位の種別:課程博士, 審査員:猪原 健弘,坂野 達郎,山元 啓史,金子 宏直,中丸 麻由子
Citation(English)	Degree:Doctor (Engineering), Conferring organization: Tokyo Institute of Technology, Report number:甲第10924号, Conferred date:2018/6/30, Degree Type:Course doctor, Examiner:,,,,
学位種別(和文)	博士論文
Type(English)	Doctoral Thesis

Systemic Properties of Dynamical Traffic Congestion

Dissertation for the Doctor of Engineering

Masaru KAJI

Thesis Adviser: Professor Takehiro INOHARA

Abstract

Traffic congestion is one of the social issues, particularly in urban areas, which can be assumed in many places such as stations, festivals, religious holidays, and highways. The characteristics of traffic congestions by simulation have been studied since 1990's. The simulations were conducted in each space shape: room, corridor, and network. In this dissertation, characteristics of traffic congestion in each case were clarified. For this, simulations focusing on pedestrian and vehicle dynamics were conducted. Factors associated to the simulation were divided into the following three simulations: 1) the motion of pedestrians that leave a room using a cellular automaton (CA) model was examined. Using the model, the motion of pedestrian in and around the congestion was analyzed and the relation between the motion of pedestrians and the time for completion of evacuation was discussed: 2) the dynamics of unidirectional pedestrian flow in a corridor was investigated. The CA model used for the analysis of the dynamics in a room was improved to compare the data of simulations with that of observation. Consequently, it was confirmed that the both output was the same result: and 3), the traffic dynamics in a network using a density-control method was investigated how congestion propagates and in what situations the congestion resolves. Using the method, the movement of congestion was analyzed and the condition when the traffic congestion resolves was theoretically provided. From the results, the theoretical values qualitatively agreed with that of simulations. Finally, from the results obtained in each case, the differences of the movements of objects, which are caused depending on the objects such as pedestrians and vehicles and the space shapes were concluded.

Acknowledgement

First, I would like to express my deepest gratitude to my supervisor, Prof. Takehiro Inohara, for allowing me to study this interdisciplinary topic and always supporting me with pertinent advice and warm encouragement. I would also like to thank Prof. Tatsuro Sakano, Prof. Hironao Kaneko, Prof. Hirohumi Yamamoto, and Prof. Mayuko Nakamaru for examining this thesis.

I would like to thank Prof. Kyoichi Kijima, Prof. Takao Terano, Prof. Yuki Sugiyama, Prof. Masaaki Sakagami, Prof. Yutaka Nakai, Dr Takahiko Ban, Dr Masayoshi Mutoh, Dr Masahito Kitamura, Dr Yosuke Kira, Noboru Nishiyama, Shimpei Koike, and the members of the Japanese Mathematical Sociology seminar, the Mathematical Society of Traffic Flow, and Terano Laboratory in Tokyo Tech for their helpful advice.

I would also like to express my gratitude to the members of Inohara Laboratory, particularly Satomi Segawa and Yuankan Huang, for helping me in multiple ways.

This work was supported by a Grand-in-Aid for JSPS Research Fellows, Grant Number 16J03284.

Finally, a special thanks go to my family for their support.

Contents

List of Figures

List of Tables

Chapter 1

Introduction

1.1 Previous research

Traffic congestion is one of the social issues, particularly in urban areas. This phenomena can be observed in many places such as stations, festivals, religious holidays (pedestrian dynamics), and highways and roads (vehicular dynamics). The traffic characteristics has been studied by experiments and simulation.

Through experiments, the traffic characteristics and the pedestrians' and drivers' behaviors have been clarified. There are three phases of traffic: free flow, synchronized flow, and jammed traffic in vehicular traffic [1] and pedestrian traffic [2, 3]. Traffic jams are triggered by an inefficient flow of pedestrians or vehicles and there is a relation between vehicle density and the traffic flow rate indicated by nonlinear characteristics [4]. That is, the flow rate increases with the traffic density; however, the flow rate decreases when the vehicle density is higher than a critical value in the traffic flow [1, 5, 6]. This phenomenon is also observed in pedestrian traffic [2, 3, 7–13]. The *stop-and-go wave* is another traffic characteristic and is a congestion cluster consisting of many vehicles [6, 14, 15] or pedestrians [10, 12, 13, 16–18]. The vehicles involved in these clusters reduce their speed and stop. They move again when the vehicles in front of them move. The wave propagates in the direction opposite to the movement of the vehicles.

Many experiments have been conducted on individual subsystems, such as highways [1, 15], ramps [4, 14], streets [2, 7–11, 13, 16, 19, 20], traffic circles [3, 6, 12, 21, 22], stairs [11], junctions [11], bottlenecks close to exits (or escapes from a room) [19, 23–27], and intersections [28, 29]. Meanwhile, the traffic dynamics were

studied by linking multiple subsystems and regarding them as a complex system (i.e. a network [5, 30, 31]) because in real-world traffic, roads are connected and form a network, and the effects of the traffic conditions on a particular road are transmitted to the adjacent roads via joints, such as intersections or junctions. To understand flow efficiency at a city-scale level, experiments were conducted in Yokohama, Japan [5]. Through the experiments, they calculated macroscopic fundamental diagrams (MFDs) that relates the average vehicle density and the average vehicle flow rate in the city. To demonstrate the flow of dynamical congestion propagation, a spatio-temporal congestion algorithm was developed, and actual and valid instances of congestion propagation in the network traffic data for an Australian city was identified [31].

Depending on the conditions of the experiments, injuries to and even death of the participants are possible in experiments, such as under high population or vehicle density. Thus, experiments cannot assume various situations because of ethical limitations. Simulations are advantageous in terms of their capability to assume various situations in a virtual space. The traffic characteristics of pedestrian dynamics by simulation have been studied since 1990's. The simulations have been conducted during evacuation from a room and movement in a corridor using a social force model [32–36], cellular automaton (CA) model [20,25–27,37–55], lattice gas model [23,56–60], fluid dynamic model [61], and optimal step model [62]. In particular, CA models [20,25–27,37–55] have advantages in terms of simplicity, flexibility, extensibility, and computational efficiency. A CA model can assume various pedestrian simulations such as evacuation from a room [37–39,42,51] and unidirectional flow in a corridor [20, 40, 44]. To assume the more realistic situation, CA models have been improved by floor field methods [41–53] and multi-grid methods [25–27, 52, 54, 55].

CA models treat a space, such as a room or a corridor, as a whole system. Meanwhile, several simulations regard traffic as a network of subsystems such as roads and intersections, and analyze the overall efficiency and congestion dynamics in the network. To predict the traffic behavior in a traffic network by integrating traffic nonlinear characteristics [1–3, 5–13], cell transmission models were developed [63–65]. In the models, a stop-and-go wave was reproduced. To analyze the MFD in a traffic network, a density-control method [66] and a simplified graph-based model [67] were developed.

1.2 Research purpose

The purpose of this dissertation is to clarify the differences of the movements of objects, which are caused depending on the objects such as pedestrians and vehicles and the space shapes such as room, corridor, and network. To investigate differences, we examine the traffic dynamics in a room, a corridor, and a network by simulation. Namely, we conclude the characteristics where congestion happens, how the congestion propagates, and what cases the congestion resolves in each system.

We focus on the traffic dynamics in a room, a corridor, and a network. We deal with the pedestrian dynamics and reproduce the pedestrians' behavior in Chapters 2 and 3. In Chapter 2, pedestrians moving freely in a space are assumed. In Chapter 3, pedestrians moving in one direction are assumed. In Chapter 4, we discuss the traffic dynamics in a network and deal with both the pedestrian and the vehicle. Note that the network is assumed to be a space consisting of multiple roads (e.g. an underground shopping area, a space in a building, or an arterial road) in this dissertation. We assume that objects which were regarded as pedestrians or vehicles move around in a network.

1.3 Structure of thesis

In the rest of this chapter, we give an overview of each chapter. Chapter 2 focuses on the motion of pedestrians that leave a room and this is simulated by an improved CA model to analyze how pedestrians move in and around the congestion near an exit. Using the CA model, Chapter 3 focuses on the unidirectional pedestrian dynamics in a corridor to reproduce the peculiar traffic phenomenon observed in a corridor. Chapter 4 focuses on the dynamics of traffic congestion in a network to investigate the traffic dynamics in the network using a density-control method. Finally, the conclusions are presented in Chapter 5.

1.4 Overview of each chapter

In Chapter 2, we focus on pedestrian evacuation in a room. Most previous studies regarding evacuation investigated the overall efficiency of evacuation for studying safe and rapid evacuation. Meanwhile, we examine the motion of pedestrians that

leave a room. If there is congestion near the exit, pedestrians in and around the congestion will attempt to approach the exit by changing their speed. That is, they will move in a zig-zag course depending on the number of people being in a room. Confirming the relation between their motions in a room during evacuation and the number of evacuees will improve understanding of efficient evacuation.

We confirm and analyze their motion in a room during evacuation in detail by simulation. To analyze their motion in congestion, we propose an improved CA model that integrates the multi-grid method and the static floor field method. Using this model, we set the form of pedestrians, their speed, their intentionality toward the exit, and the form of the room for a more realistic situation. We then conduct simulations, namely, we place pedestrians in the room and let them move toward the exit. From the results, we analyze the relation between the time for completion of evacuation and the initial number of pedestrians in the room. We also discuss the relation between the initial number of pedestrians and their motion during evacuation.

In Chapter 3, we deal with the unidirectional pedestrian dynamics in a corridor. In experiments conducted in a shopping street and on a bridge [13, 16], a peculiar phenomenon was observed. The velocity profile in the corridor was a parabolic curve, in which the velocity was smaller as the wall of a corridor was approached closer. The density profile in the corridor was a downward convex parabolic curve. That is, the population density was larger as the wall of a corridor was approached closer. This may be attributed to the fact that the walls have attractive factors, such as booths and a beautiful landscape visible from the bridge. Although the factors that cause this phenomenon have not yet been clearly demonstrated, it is assumed that there is a factor that causes pedestrians to attempt to move toward the walls. As a result, inefficient flow because of high density may occur near the walls and average speeds decrease.

We conduct simulations under a hypothesis and confirm whether the pedestrians' velocity profile is reproduced. The hypothesis is that pedestrians have intentions to move towards the wall side, that is, they attempt to walk along the wall side as much as possible. To express the hypothesis, we use the CA model with the multi-grid method and static floor field method in Chapter 2. We improve the model by incorporating the pedestrians' personal spaces and headways for a more realistic situation. We set a corridor and unique static floor fields that

express pedestrians' intention toward the wall. We then let pedestrians move in the corridor and calculate the velocity profile. From the results, we investigate the relation between the form of static floor field and the velocity profile and compare the results with the experimental results [13, 16]. Thereby, we judge whether our hypothesis is correct. We also discuss the necessity of the personal space and headway by comparing results that integrate the personal space and headway with those that do not integrate these parameters.

In Chapter 4, we focus on the traffic dynamics in a network. In previous research [66], a density-control method was developed and integrated a nonlinear traffic characteristic into a defined network. In addition, on–off control rules such as traffic light control [68] were adopted. Thereby, the efficiency of traffic flow in the network was discussed and it was confirmed that there were three phases in the network: free flow, controlled, and deadlock. They also qualitatively analyzed the boundary condition between controlled and deadlock phases, namely, the condition for breakdown of the system. However, they did not confirm how the existing traffic jam specifically affects the adjacent roads. In real-world traffic, the paths for pedestrian movement and the roads for vehicles are connected and extend in a network through intersections or junctions. In the network, it is assumed that a cluster such as a stop-and-go wave propagates to the adjacent roads and affects other vehicles or pedestrians. Determining whether the wave cluster affects the other adjacent roads will be useful to predict when, where, and how seriously the traffic congestion affects a certain road.

We investigate how the existing traffic jam specifically affects the adjacent roads and subsequently resolves in a network. To confirm the dynamics, we use the density-control method [66]. In previous research, a 10-regular directed closed graph was used; in contrast, we use a cubic directed closed graph (a 3-regular directed closed graph) for a more realistic road network. We set a steady state (i.e. an inflow in an arc is the same as the outflow in the arc) by setting all arcs with a uniform density. We then intentionally generate a traffic jam in an arc and conduct simulations. Next, we observe how the congestion moves in the network or resolves. Subsequently, we theoretically deprive the condition when the traffic congestion resolves in the network. That is, the boundary condition between free-flow and controlled phases. We then compare the theoretical values with the simulation results and discuss the difference between our results and the

previous results [66]. We finally show the usefulness of the method.

Chapter 2

Evacuation simulation of a square room

In this chapter, we focus on the motion of pedestrians that leave a room and examine how pedestrians moved in and around the congestion near an exit. In the case of a congestion near the exit, each pedestrian in and around the congestion will change their speed and course to approach the exit. That is, a pedestrian will move in a zig-zag course in the congestion. To analyze their motion in congestion, we set a CA model with a multi-grid method and a static floor field method. Using the model, we observe pedestrians' motions in the room. We analyze the relation between the time for completion of evacuation and the initial number of pedestrians. We qualitatively compare our results with the results of the other simulation model and discuss the usefulness of our model.

Detailed simulation rules of this method are introduced in the next section. Section 2.3 shows the simulation results, while Section 2.4 presents conclusions.

2.1 Methods

2.1.1 CA models

CA models deal with time and space, which are discretized into even intervals. A space is expressed by small squares, called cells [20, 25–27, 37–55]. In CA models expressing pedestrian dynamics, a cell is assumed to be a pedestrian, an obstacle, or an empty space. Pedestrians stochastically move to an adjacent cell according

to a set of local rules. Typical CA models have advantages in terms of the ability to reproduce the pedestrian motion and the form of space.

2.1.2 Multi-grid methods

To obtain a more realistic reproduction of pedestrians' movement, three existing problems of CA models should be solved. First, in conventional CA models, a square cell is regarded as a pedestrian (Figure 2.1(a)), which is a major simplification. Second, a pedestrian can move in only four directions in the Neumann neighborhood or eight directions in the Moore neighborhood, namely, they move horizontally, vertically, or diagonally. Hence, they are limited in their moving direction. Third, a pedestrian can move only to adjacent cells; that is, they must move at a fixed speed.

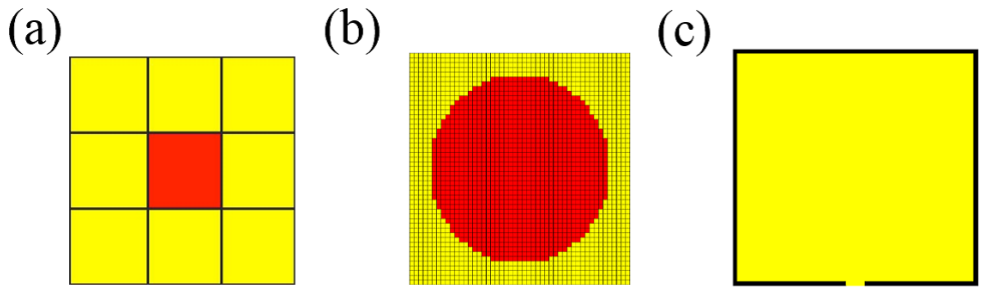

Figure 2.1: (a) A pedestrian in a conventional CA model. Red: pedestrian; yellow: empty space. (b) A pedestrian used in this simulation. Red: body of the pedestrian; yellow: empty space. (c) Square room used in this simulation. Black: wall; yellow: area of the room in which a pedestrian can exist; exit: center of the lower region.

Multi-grid methods [25–27,52,54,55] that constitute a type of CA model were developed to overcome the three disadvantages of conventional CA models. In these methods, we divided a cell finely and regarded the connected multiple cells as a pedestrian. That is, a space is discretized into cells smaller than in conventional CA methods as shown in Figure 2.1(b). Thus, we can more realistically define the form of a pedestrian, a pedestrian's size, direction of a pedestrian's movement, a pedestrian's speed, and the width of exits. Multi-grid methods are

one of the most reproducible methods because many simulation results obtained from multi-grid methods agreed with the experimental results [25–27, 55]

We expressed a pedestrian and a square room in detail using this method. Let a cell (x, y) have position coordinates, where x and y are the lateral and longitudinal coordinates, respectively ($x, y \in \mathbb{N}$). A cell (x, y) was defined as part of the pedestrian i if cell (a, b) was the center of the pedestrian i, and if the distance from cell (x, y) to cell (a, b) was smaller than the radius r of i, namely,

$$\sqrt{(a-x)^2 + (b-y)^2} < r. \tag{2.1}$$

We defined a cell as a square with sides of 1.25 cm. We also assumed that the radius r was 20 cells (i.e. a pedestrian had a diameter of approximately 50 cm).

In this simulation, we set a square room. The room was a 2000 rows by 2000 columns grid (i.e. a square with sides of approximately 25 m, Figure 2.1(c)). The room was surrounded by walls, and an exit was located at the center of the low region. The width of exit d was 2 m (or 160 cells wide). The pedestrians were placed randomly, and the simulation made them exit the room.

2.1.3 Floor field methods

Floor field methods [41–53] were also used in this simulation. The methods were separated into two types: static floor field methods [41–52] and dynamic floor field methods [49–53]. Static floor field methods introduce the destination preferences; hence, they can simulate evacuation from a complex space with obstacles. In dynamic floor field methods, a pedestrian unfamiliar with the destination attempts to follow others by introducing virtual pheromones, which is analogous to the use of formic acid by ants. We used a static floor field method because we assumed that all the pedestrians have accurate knowledge of the room and the destination. The static floor field method expresses the intention of each pedestrian. If a pedestrian is placed in the left-hand side of the room, they attempt to move to the lower right-hand side as shown in Figure 2.2(a). We defined each cell's number from the goal to equip the pedestrians with the intentionality to go toward the exit. The pedestrians attempt to move to a cell, whose number is smaller than that of the present cell. As shown in Figure 2.2(b) and (c), we defined the number of the cell at the center of the exit as a value of 1. The value of a

cell (x, y) was denoted by $S(x, y)$, which is the distance from the center of the exit to the cell (x, y). Previous studies assumed a static floor field to be a Manhattan matrix as shown in Figure 2.2(b) [49, 50] or improved matrices [41, 43, 45–48]. In contrast, for a more realistic reproduction, we assumed that a static floor field was a Euclidean distance matrix as shown in Figure 2.2(c). That is, the value $S(x, y)$ of a cell (x, y) was defined as the following integer:

$$S(x, y) = \lceil \sqrt{(x - x_e)^2 + (y - y_e)^2} + 1 \rceil, \tag{2.2}$$

where $\lceil x \rceil = \min\{n \in \mathbb{Z} \mid x \leqslant n\}$. x_e and y_e are the lateral and longitudinal coordinates at the center of the exit, respectively. In Equation (2.2), 1 was added to the Euclidean distance to set the value of the cell nearest to the exit cell. The value of $S(x, y)$ was rounded off to the nearest integer. Note that the value was not calculated for the walls because the pedestrians do not pass through a wall. We defined the static floor field of pedestrian i at t on cell (x_i^t, y_i^t) as S_i^t. Here, x_i^t and y_i^t denote the lateral and longitudinal coordinates at the center of i at t, respectively. Note that the value of S_i^t was equal to the value $S(x_i^t, y_i^t)$. Pedestrians are required to move from a cell with a bigger value to a cell with a smaller value. In other words, they attempt to move toward the center of the exit. When pedestrian i moves at speed $V_i(t)$ at t,

$$S_i^{t+1} = S_i^t - V_i(t). \tag{2.3}$$

In previous studies [41–53], the pedestrians were made to move probabilistically using a static floor field. In contrast, in our simulation, the pedestrians moved deterministically.

2.1.4 Algorithm of the simulation

In this section, the algorithm for pedestrians in our simulation is described. Then, the initial state, the parameters, and the moving and updating procedures for pedestrians are defined. Finally, the entire algorithm of the simulation is explained.

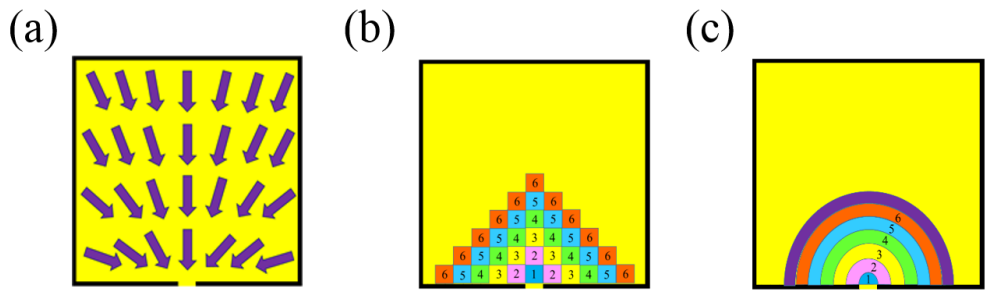

Figure 2.2: (a) Intentionality of the pedestrians in the room. The arrows are the direction, in which the pedestrian attempts to move. (b) Static floor field of a room consisted of a Manhattan matrix [49, 50]. (c) Semi-circular static floor field of a room in our simulation.

2.1.4.1 Algorithm for pedestrians

As the initial state of pedestrians, we randomly placed all the pedestrians in the room as shown in Figure 2.3 using the Monte Carlo method. Next, the pedestrians move toward the exit by updating S_i^t, which is the static floor field of pedestrian i at t. The algorithm for the movement of pedestrian i is given in Algorithm 1. Pedestrian i attempts to move at their ideal speed V_{ideal}. If i cannot move at their ideal speed, they reduce their speed $V_i(t)$. If i can move at $V_i(t)$, they move there and S_i^t is updated according to Equation (2.3). If i cannot move because of other pedestrians or walls, i stands in place, that is, $V_i(t) = 0$ and $S_i^{t+1} = S_i^t$. Then i is removed from the simulation when $S_i^{t+1} = 0$, namely, i arrives at the exit. We set all the pedestrians' ideal speeds to 40 cells ($V_{ideal} = 40$) for one time step (i.e. all the pedestrians attempt to walk at 1.0 m/s (3.6 km/h) or less).

2.1.4.2 Entire algorithm

Algorithm 2 denotes the entire algorithm in this simulation. First, we defined the square room and the static floor field. Second, the time step was initialized as $t = 0$, and the pedestrians were placed randomly in the room. Third, t was updated (i.e. pedestrians started to move toward the exit at $t = 1$). Each pedestrian was moved in an order based on Algorithm 1. Then t was updated after all the pedestrians in the room were updated. This simulation was conducted

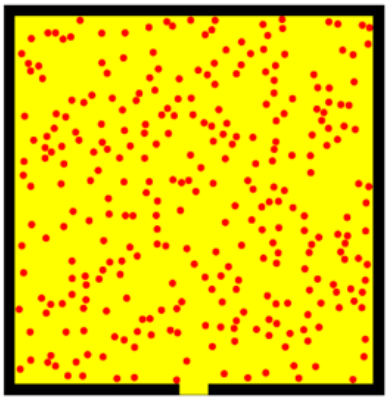

Figure 2.3: Pedestrians randomly placed in the room. Red cells denote pedestrians. A total of 300 pedestrians are in the room.

until all the pedestrians were evacuated from the room.

Here, we define the updating procedure for moving pedestrians. We can think of the following three procedures: parallel, shuffled sequential, and ordered sequential procedures. It seemed natural that pedestrians were updated in turn according to their distances from the exit. This is because when the pedestrians form a queue, one pedestrian cannot move forward if the person ahead does not move forward. In fact, a previous study on this updating procedure [25] compared various updating procedures and showed that the ordered sequential procedure can obtain better results. Hence, we adopted the ordered sequential procedure. Collisions did not occur because of the sequential update.

The updating procedure in [25] was used on a triangular update field spreading from the center of the exit as shown in Figure 2.2(b). Meanwhile, for more realistic assumption, we used the procedure on the improved Euclidean distance matrix as shown in Figure 2.2(c). The value of the distance in the updating procedure of the simulation agreed with that of the static floor field $S(x, y)$. The pedestrians with the same distance are updated randomly.

Algorithm 1 Movement of pedestrian i at t

Require:

i: a pedestrian in a room moved by this algorithm
t: time step
S_i^t: static floor field of pedestrian i at t
$V_i(t)$: speed of pedestrian i at t
V_{ideal}: ideal speed of a pedestrian
k: parameter for confirmation execution

Ensure: : End of run if $k = 1$, namely, update the place of i from at t to at $t + 1$

$k \leftarrow 0$
$V_i(t) \leftarrow V_{ideal}$
while $(k = 0)$ **do**
  if there is movable place in $V_i(t)$ **then**
    Let i move there
    $S_i^{t+1} = S_i^t - V_i(t)$
    if $S_i^{t+1} = 0$ **then**
      Delete i from the room
    end if
    $k = 1$
  else
    $V_i(t) \leftarrow V_i(t) - 1$
  end if
  if $V_i(t) = 0$ **then**
    $S_i^{t+1} = S_i^t$
    $k = 1$
  end if
end while

2.2 Results

2.2.1 Formation of semi-circular congestion

Figure 2.4 illustrates the state in the room when the initial number of pedestrians was 300. The red cells denote pedestrians, the yellow cells are empty spaces, and the black cells are walls. Semicircular congestion is occurring near the exit.

2.2.2 Zig-zag motion and detour motion in and around the congestion

Figure 2.5 shows the streamlines of pedestrians for the case with different initial number of pedestrians: 30, 70, 150, and 300 at $t = 50$. The results implied that most of the streamlines linearly occurred toward the exit when there were fewer

Algorithm 2 Entire algorithm for evacuation

Require:
i: a pedestrian in a room
t: time step
T: time for completion of evacuation
n: the number of pedestrians in a room
N: the initial number of pedestrians
S_i^t: static floor field of pedestrian i at t
s: distance from a position to the exit
S_{MAX}: maximum value of static floor field
Ensure: : Calculate T
Define space
Define static floor field according Equation (2.2)
Place N pedestrians in space randomly
$t \leftarrow 0$
$n \leftarrow N$
while $(n > 0)$ **do**
  $S \leftarrow 1$
  while $(s < S_{MAX})$ **do**
    for all i such that $S_i^t = s$ **do**
      Execute Algorithm 1
    end for
    $s \leftarrow s + 1$
  end while
  Count n in the room
  $t \leftarrow t + 1$
end while
$T = t$

pedestrians placed initially. If the initial number of pedestrians is higher, many of their trajectories are not linear. That is, the pedestrians who were located farther from the exit in the room evacuate while moving in a zig-zag course in front of the exit.

Figure 2.6 indicates the velocity vector fields when the initial number of placed pedestrians is 100 at $t = 0$, 10, 20, 30, 40, and 50. The red arrows show the velocity vectors, and the length of the arrow represents the pedestrian's velocity. From the results, we found that the velocity of a pedestrian in front of the exit is low. A pedestrian behind another pedestrian, who can go forward at a high speed, can also go ahead at a high speed because a pedestrian near the end of the

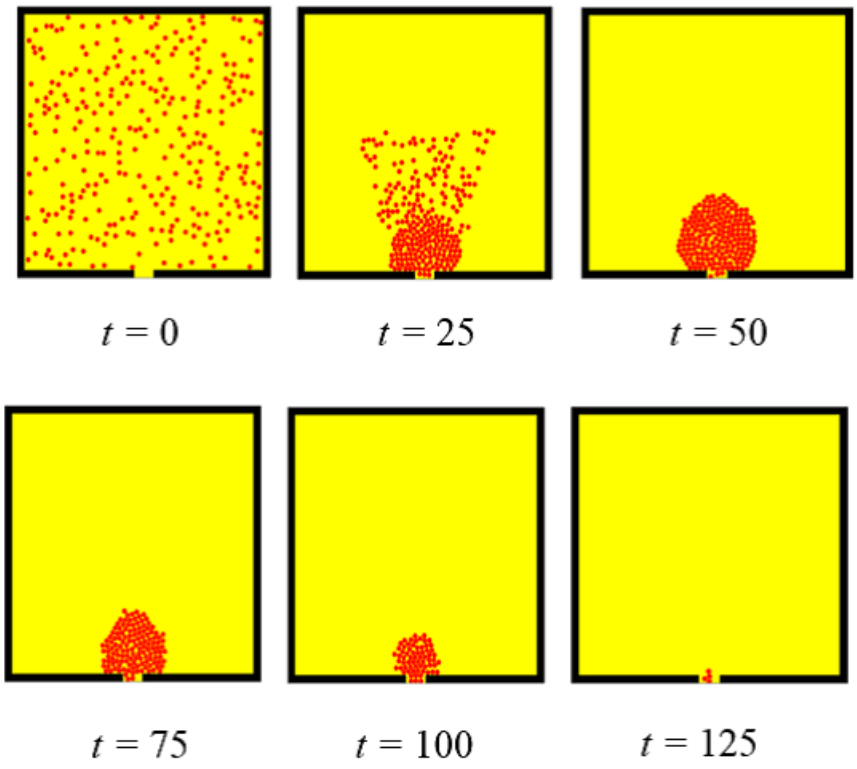

Figure 2.4: State in the room at $t = 0$, 25, 50, 75, 100 and 125. The initial number of pedestrians is 300. The ideal speed of the pedestrians is 40 cells.

congestion near the exit attempts to detour to avoid the congestion and approach the exit as quickly as possible.

2.2.3 Time for completion of evacuation

Figure 2.7 presents the relation between the initial number of pedestrians and the time for completion of evacuation. For each initial number of pedestrians, simulations were conducted 10 times, and the average time and variance were calculated. The time for completion of evacuation increased monotonically as the initial number of pedestrians increased. Figure 2.7 presents three phases: large variance phase (I), stable phase (II), and linear phase (III). In phase I, the scale bar when the initial number of pedestrians was fewer than approximately 30 was

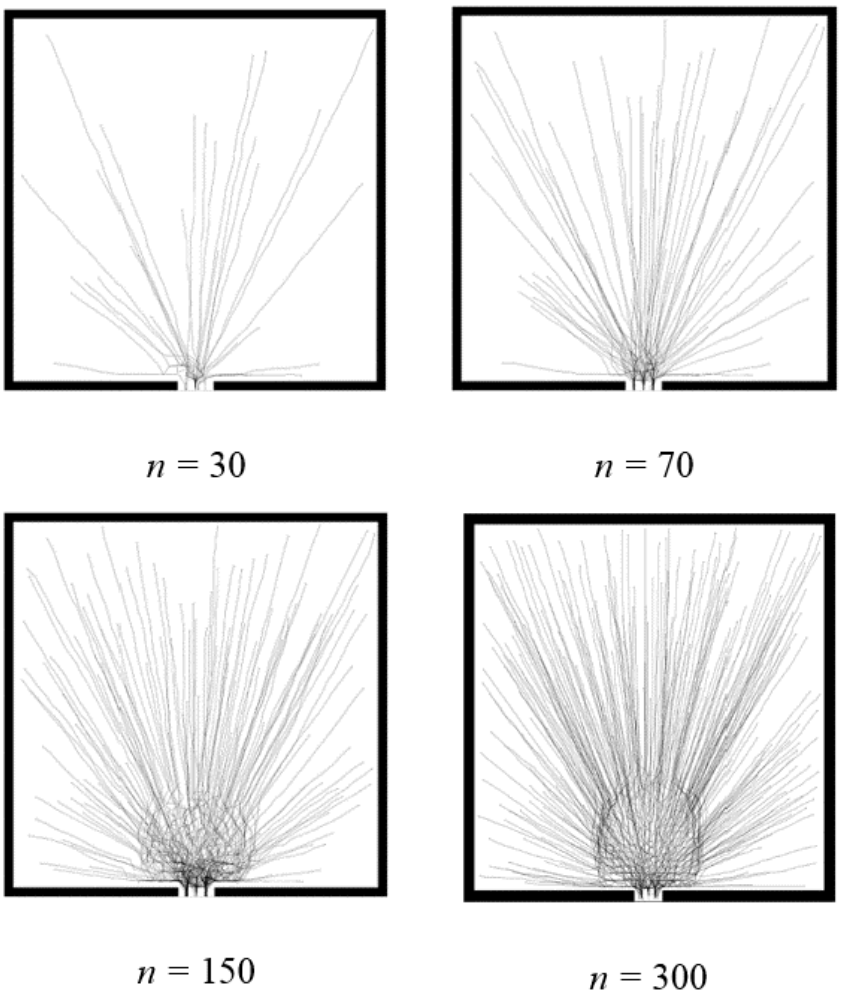

Figure 2.5: Streamline of pedestrians. The initial number of pedestrians is 30, 70, 150, and 300. The ideal speed of a pedestrian is 40 cells. The time step is 50.

comparatively wide (i.e. the value of the variance was large) because the time for completion of evacuation heavily depended on the distance of the farthest pedestrian from the exit. In phase II, the value of time for completion of evacuation became stable when the number of pedestrians ranged from approximately 30 to 80. In phase III, the time for completion of evacuation linearly increased when

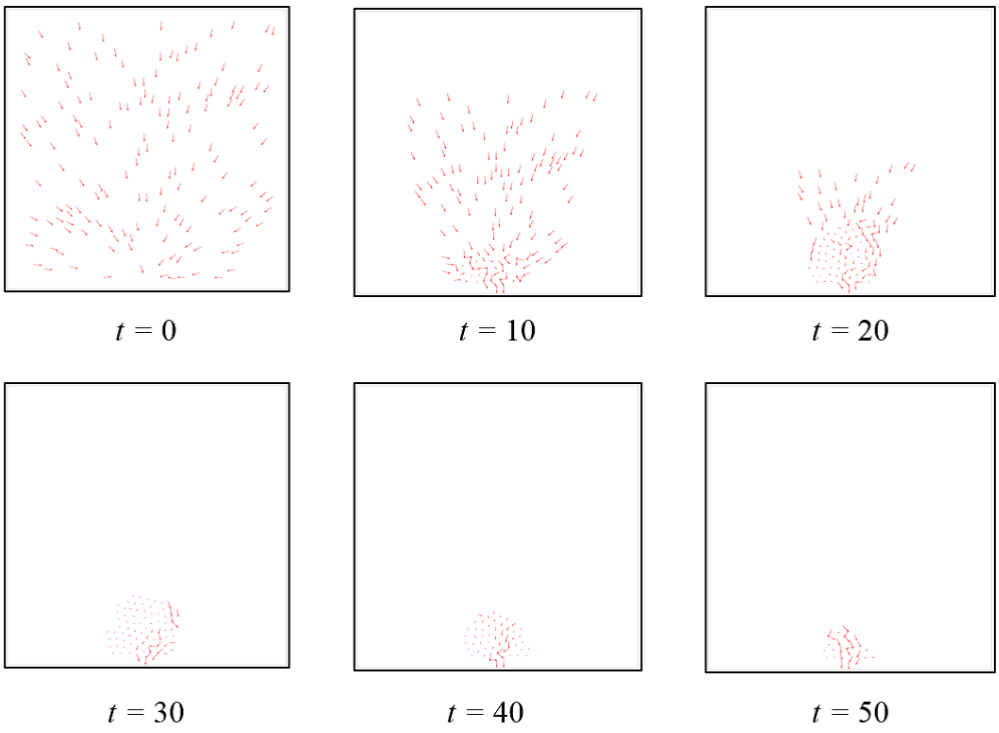

Figure 2.6: Velocity vector fields of the pedestrians when the initial number of pedestrians is 100 and at $t = 0$, 10, 20, 30, 40, and 50.

the initial number of pedestrians was over 80. We confirmed that a semi-circular congestion definitively occurred in phases I and II.

Figure 2.8 shows the relation between the initial number of pedestrians and the time for completion of evacuation in the case of changing d. From the results, we found that the time for completion of evacuation monotonically increased as the initial number of pedestrians increased regardless of the width of exit d. The time for completion of evacuation in each d when the initial number of pedestrians was fewer than approximately 30, was almost same value regardless of d. In each case, the time for completion of evacuation increased linearly when the initial number of pedestrians was comparatively large.

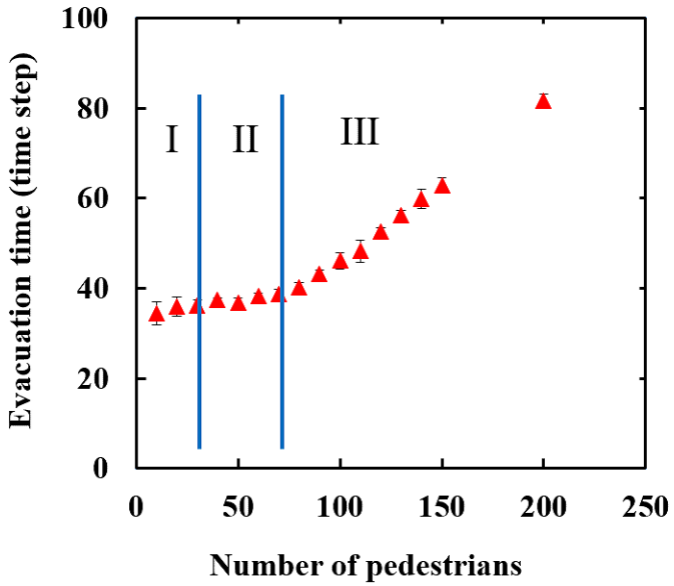

Figure 2.7: Relation between the time for completion of evacuation and the number of pedestrians. Phases I, II, and III denote the large variance, stable, and linear phases, respectively.

2.3 Discussion

In Figure 2.5, we confirmed that pedestrians involved in congestion moved in a zig-zag course when there is semi-circular congestion in front of the exit. We observed this motion during the stable phase (II) and the linear phase (III). In the large variance phase (I), the pedestrians could go straight toward the exit and leave the room. That is, the critical value between phases I and II provides an indication of quick and safe evacuation. In phase II, the value of time for completion of evacuation became stable regardless of the initial number of people. Therefore, evacuation in phase II will be achieved within a certain time if there no crowd disaster occurs because of physical contact and panic. Evacuation in phase III is higher risk than that in phases I and II. In a previous CA method [42], Yamamoto and colleagues showed that there are two regions: a region in which time for completion of evacuation is constant and no congestion is formed; and a region in which the time for completion of evacuation increases when the initial number

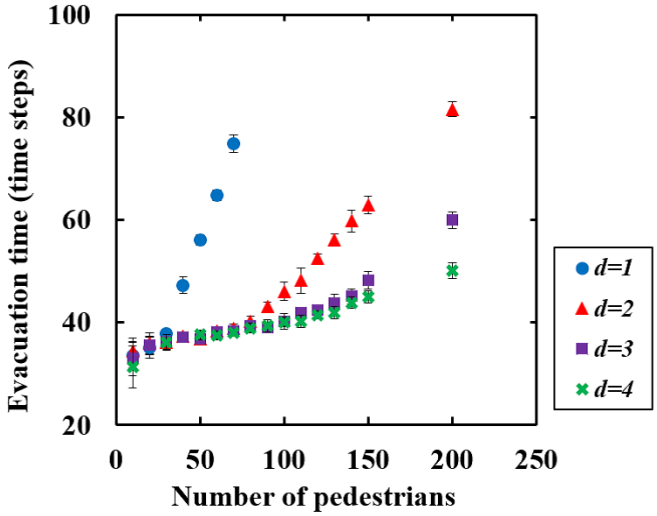

Figure 2.8: Relation between the time for completion of evacuation and the number of pedestrians in the case of changing the width of exit d. The results of $d = 2$ in this figure correspond to results in Figure 2.7.

of pedestrians increases and congestion is observed. They did not indicate their pedestrians' motion in the simulation. Meanwhile, in our simulation, we clarified the three qualitatively different phases in evacuation simulation and reproduced the pedestrians' motion.

2.4 Conclusions

We have examined how pedestrians move in and around the congestion near an exit. To analyze their motion, we developed a CA model with a multi-grid method and a static floor field method. Using the model, we reproduced a semi-circular congestion near the exit. We observed the relation between the time for completion of evacuation and the initial number of pedestrians and found three phases: large variance (I), stable (II), and linear phases (III). Based on the differences of each phase, we clarified the characteristic of pedestrians' motions. In phase I, the pedestrians moved straight toward the exit because there were few pedestrians in the room. The time for completion of evacuation depends on

the distance of the farthest pedestrian from the exit. Pedestrians involved in congestion moved in a zig-zag course and detoured in and around the congestion in phases II and III. We could show the usefulness of our model by comparing our results with results of a previous simulation model.

In the following chapter, we discuss pedestrians' unidirectional flow. In Chapter 2, pedestrians who move freely in a room were assumed. In Chapter 3, pedestrians who move in one direction are assumed for the sake of comparison. We also reproduce the congestion occurring in a corridor by improving the simulation method used in this chapter. In the simulation, velocity profiles and density profiles are analyzed.

Chapter 3

Simulation of the unidirectional pedestrian flow in a corridor

In the previous chapter, we focused on the motion of pedestrians that leave a room. The movement of pedestrians in and around the congestion near an exit were discussed. In this chapter, we focus on the unidirectional pedestrian dynamics in a corridor to reproduce experimental results [13, 16] using our simulation methods. In the experiments [13,16], the peculiar velocity profiles of pedestrians in a corridor were observed. That is, the velocity profile is a parabolic curve, in which the velocity is smaller as the wall of a corridor is approached. To reproduce the velocity profile, we hypothesize that pedestrians attempt to walk along the wall side as much as possible. Thereby, many people attempt to go toward the wall side and, consequently, traffic congestion occurs there and average speeds decrease. We examine whether the hypothesis is correct using a CA model with the multi-grid and static floor field methods. We improve the model presented in Chapter 2, incorporating the pedestrians' personal spaces and headways into the model for a more realistic situation. Using the model, we set a corridor and unique static floor fields that integrate pedestrians' intention toward the wall. We then move pedestrians in the corridor and calculate the velocity and density profiles. From the results, we discuss the relation between the form of static floor field and the velocity profile and compare the results with the experimental results [13,16]. We also discuss the differences between results that integrate the personal space and headway and results that do not integrate these parameters.

The various simulation rules of the improved CA model are described in the

next section. Section 3.3 compares the results with those from a previous study and Section 3.4 presents conclusions of this chapter.

3.1 Methods

In this section, we first set a multi-grid, then define a static floor field. Finally, we developed the algorithm of simulations.

3.1.1 Multi-grid methods

We used a multi-grid model [25–27, 52, 54, 55] in Section 2.1.1. We considered not only pedestrians' shape and moving speeds, but also personal spaces and headways using the multi-grid method.

3.1.1.1 Cell size

We defined the form of a cell as a square with 3 cm sides. We made a nearly circular shape by combining many cells and regarded the complex as a pedestrian as shown in Figure 3.1. We assumed that the radius was approximately $3r$ cells (i.e. a pedestrian had a diameter of approximately r cm). We assumed that cell (a, b) was the center of the pedestrian i. The cell (x, y) was considered part of pedestrian i if the distance from cell (x, y) to cell (a, b) is smaller than the radius of pedestrian i, i.e.,

$$\sqrt{(a-x)^2 + (b-y)^2} < r, \tag{3.1}$$

where, we fixed the body size to 39 cm (= 13 cells). Note that the cell size discussion was given in Section 3.2.2.

3.1.1.2 Pedestrians' speed

We defined that all the pedestrians had the same ideal speed V_{ideal} m/s. Pedestrian i reduces speed or changes direction if it is possible to move when another pedestrian occupies the place to which pedestrian i attempts to move. A detailed explanation of a pedestrian's movement is given in Section 3.1.3.1.

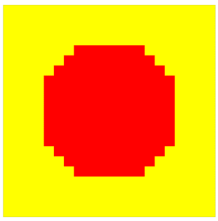

Figure 3.1: A pedestrian used in this simulation. The red cells are the body of the pedestrian and the yellow cells are empty cells.

3.1.1.3 Personal space and headways for pedestrians

We set personal spaces and headways for pedestrians. A few CA methods reflected this fact despite the fact that a simulation model had integrated personal space [62] and several experimental studies reported on personal spaces and headways in pedestrian dynamics [3, 12, 22]. For a more realistic reproduction, we may need to integrate personal spaces and headways into the simulation. This is why we integrated personal spaces and headways. We compare results that do not integrate personal space with those that integrate personal space in Section 3.2.2.

A person feels discomfort when their personal space is encroached upon. As shown in Figure 3.2, personal space is divided into four types: intimate, personal, social, and public [69]. The area of the intimate space is within the limits of approximately 45 cm and is the smallest of the four spaces. An intimate person, such as a lover, a close family member, or a familiar friend, is permitted to encroach into this space. Its close region (<15 cm) is the area in which a person can hold others. Its far region (15–45 cm) is the area in which a person can perform a light touch with their hands. A personal space in the range of 45–120 cm is used during conversations. The social space ranges from 120 to 360 cm, and is outside the purview of 360 cm. For simplicity, we integrated only the close region of the intimate space in this simulation. We assumed that the personal space of pedestrian i was 15 cm.

We integrated headways into the pedestrian model. As shown in Figure 3.3, the formation of a personal space resembles the shell of a snail [70]. A sharp point corresponds to the headway of a pedestrian. The relation of headways and pedestrian walking speeds through experiments were studied in [12]. The authors

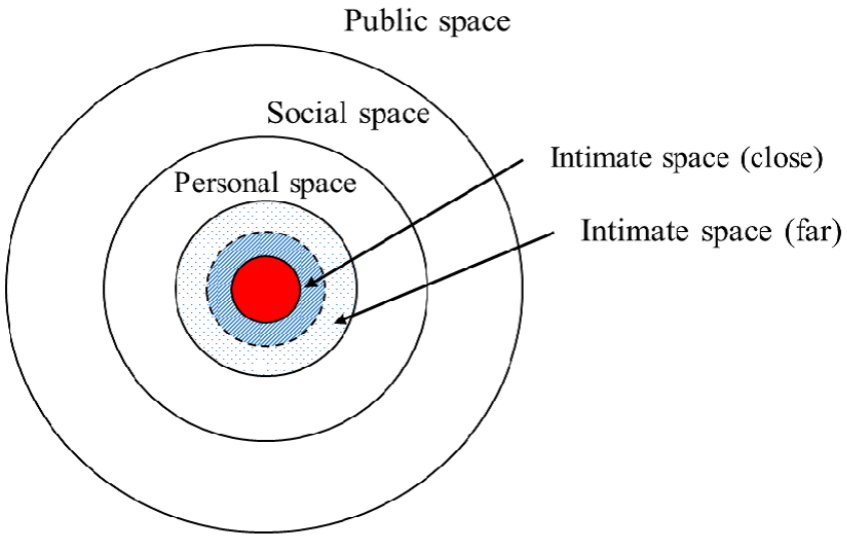

Figure 3.2: Diagram of personal space [69]. We consider the close intimate space (blue area) in this chapter.

showed that the pedestrians tend to increase the spatial headways as pedestrians' speed linearly increases. Based on the previous results [12], we assumed a piecewise linear function $H(V_i)$ (in meters) for the headways of pedestrian i when they move at speed V_i:

$$H(V_i) = \begin{cases} 1.01V_i + 0.37 & (V_i < 0.8), \\ 4.22V_i - 2.28 & (0.8 \leq V_i < 1.3), \\ 3.20V_i & (1.3 \leq V_i). \end{cases} \tag{3.2}$$

We assumed that a pedestrian attempted to prevent other pedestrians from entering their personal space. Figure 3.3 shows the personal space of a pedestrian consists of a circle of intimate space and a triangle of the headway in this simulation.

3.1.1.4 Corridor

Figure 3.4 describes a corridor used in this simulation. The corridor's width and length were W and L_α (area α), respectively. Both sides of the corridor were walls. Pedestrians were generated in area α or area β, whose length was L_α and

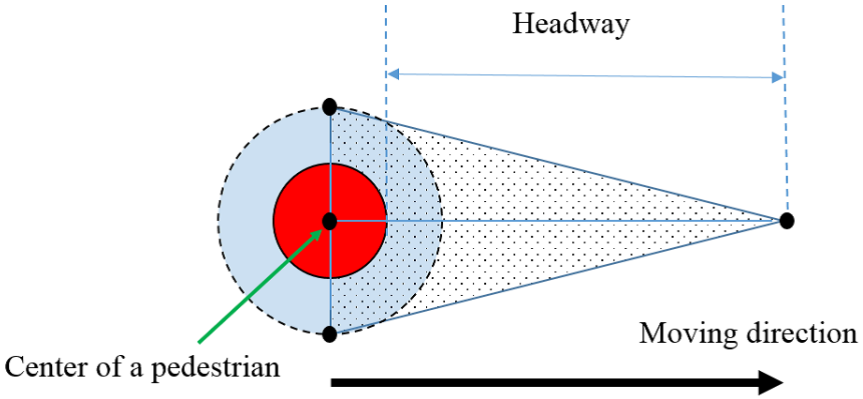

Figure 3.3: Diagram of the personal space formulation. We regard the personal space of a pedestrian as the area in the blue circle and the triangle connecting to the dot ahead.

L_β, respectively. They aimed to reach area β', whose length was L_β, through area α. In other words, the pedestrians moved from the left area to the right area. Area β was identified with area β' to generate a periodic boundary condition. We defined the direction of the length of the corridor as the x-direction and the direction of the width of the corridor as the y-direction. The length of L_α and L_β were approximately 666 cells ($\simeq$20 m) and 66 cells ($\simeq$2 m), respectively. Therefore, the total length of the corridor was 798 (= 66 + 666 + 66) cells. The corridor width was 333 cells ($\simeq$10 m) to allow a comparison with the results in [13].

3.1.2 Floor field methods

A static floor field method in a corridor was defined. To confirm the velocity profile in various situations, four types of floor fields were assumed as shown in Figure 3.5. Pedestrians attempted to move from the red cell to the orange, yellow, yellowish green, sky blue, blue, and purple cells. The pedestrians attempted to cross the contour lines. That is, in pattern A, pedestrians' intension was not integrated. In pattern B, the pedestrians attempted to move from the left to the right going towards a wall. Pattern C expressed that the intentions of the

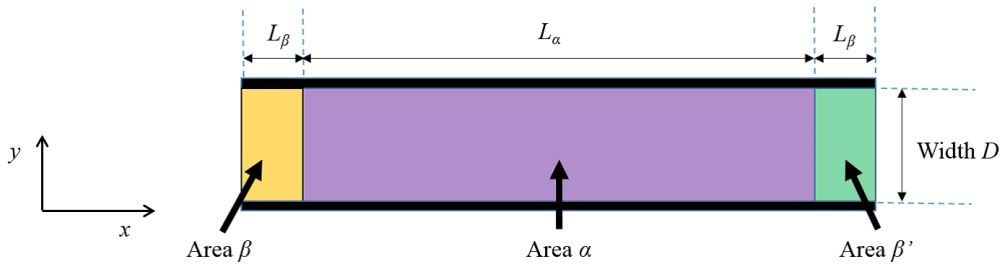

Figure 3.4: Configuration of the corridor in our simulations. We identified area β and area β'.

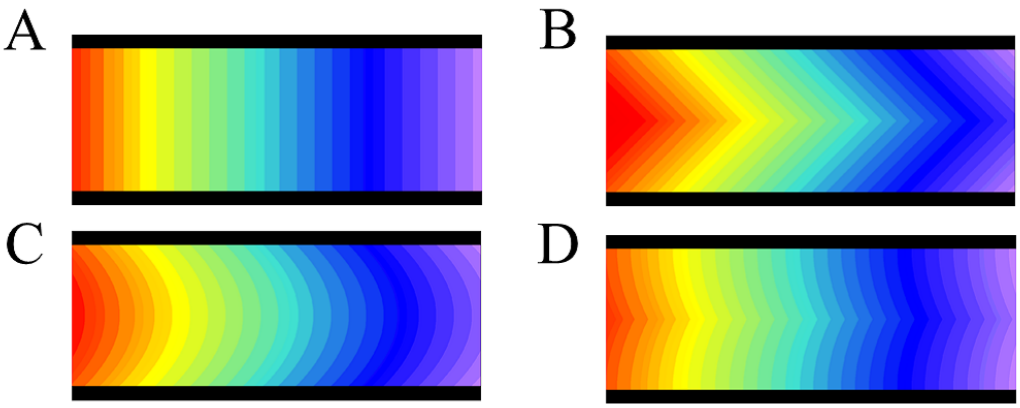

Figure 3.5: Contour lines of the static floor field.

pedestrians increase as they approached a wall. In pattern D, the intentions of the pedestrians waned as they approached a wall side. We defined $S_A(x, y)$, $S_B(x, y)$, $S_C(x, y)$, and $S_D(x, y)$ as the value of the static field in patterns A, B, C, and D, respectively. We assumed that the bottom left corner of area β had coordinates $(1, 1)$ and the value of static floor fields at coordinates (x, y), $S_A(x, y)$, $S_B(x, y)$, $S_C(x, y)$, and $S_D(x, y)$ for patterns A, B, C, and D are respectively determined as shown Algorithm 3. $\mathrm{ceil}(x) = \min\{n \in \mathbb{Z} \mid x \leqslant n\}$ and $\mathrm{floor}(x) = \max\{n \in \mathbb{Z} \mid n \leqslant x\}$. Here a is a constant ($a \in \mathbb{R}$) and expresses the strength of pedestrians' intentions to attempt to move toward a wall. The value was not calculated for the walls because the pedestrians do not pass through a wall. Pedestrians attempted to move closer to a wall as a was larger. For simplicity, we assumed that $a = 1$.

We conducted simulations in the case of changing a in Section 3.2.2.

Algorithm 3 Setting of floor field

Require:

x: coordinate of the direction of the length of the corridor
y: coordinate of the direction of the width of the corridor
x_{MAX}: maximum value of x
y_{MAX}: maximum value of y
L_α: length of in Area α
L_β: length of in Area β
W: width of the corridor
$S_A(x, y)$: value of static floor field at (x, y) of patten A
$S_B(x, y)$: value of static floor field at (x, y) of patten B
$S_C(x, y)$: value of static floor field at (x, y) of patten C
$S_D(x, y)$: value of static floor field at (x, y) of patten D

Ensure: : Determine values of floor field in Pattern A, B, C, and D

$x \leftarrow 1$
$y \leftarrow 1$
while $(x < x_{MAX})$ **do**
  while $(y < y_{MAX})$ **do**
    $S_A(x, y) = L_\alpha + L_\beta - x + 1$
    $S_B(x, y) = L_\alpha + L_\beta - x - \mathrm{abs}(y - \mathrm{ceil}(W/2)) + \mathrm{ceil}(W/2)$
    $S_C(x, y) = L_\alpha + L_\beta + \mathrm{floor}(a(\mathrm{ceil}(W/2))^2/W) - \mathrm{floor}(a((\mathrm{ceil}(W/2) - \mathrm{abs}(y - \mathrm{ceil}(W/2)))^2/W)) + 1$
    $S_D(x, y) = L_\alpha + L_\beta - x + a\mathrm{floor}((\mathrm{ceil}(W/2) - \mathrm{abs}(y - \mathrm{ceil}(W/2)))^2/\mathrm{ceil}(W/2))$
  end while
end while

S_i^t denotes the value of the static field at the coordination of the center of pedestrian i at t. Then, a pedestrian attempted to move from a cell with a larger value to a cell with a smaller value of the static floor field (i.e. attempt to move from the left to the right). When pedestrian i moved at speed $V_i(t)$ at t, the static floor field of i at $t + 1$ was moved deterministically as follows:

$$S_i^{t+1} = S_i^t - V_i(t). \tag{3.3}$$

3.1.3 Algorithm of the simulation

The algorithm used in our simulation is described in this chapter. We set an algorithm for pedestrians and an algorithm for the entire simulation.

3.1.3.1 Algorithm for pedestrians

Pedestrian i attempted to move at t as shown in Algorithm 4. There are two differences between Algorithms 1 and 3. The first is to consider personal space and headway in Algorithm 4. Pedestrians attempt to move while preventing other pedestrians from entering their personal space as stated in Section 3.1.1.3. Here $H(V_i)$ was determined before i attempted to walk in V_i according to Equation (3.2). The other difference is that a pedestrian who arrived at the exit was deleted in Algorithm 1, meanwhile, a pedestrian who arrived at area β' was moved in area β in Algorithm 4. We assumed the time difference to be 0.5 seconds in this simulation.

Algorithm 4 Movement of pedestrian i at t

Require:
i: a pedestrian in a room moved by this algorithm
t: time step
S_i^t: static floor field of pedestrian i at t
$V_i(t)$: speed of pedestrian i at t
V_{ideal}: ideal speed of a pedestrian
k: parameter for confirmation execution
Ensure: : Update S_i^t and end of run if $k = 1$
$k \leftarrow 0$
$V_i(t) \leftarrow V_{ideal}$
while $(k = 0)$ **do**
  Calculate $H(V_i)$
  if there is movable place in $V_i(t)$ **then**
    $S_i^{t+1} = S_i^t - V_i(t)$
    $k = 1$
    if there is i in area β' **then**
      Move i area β
    end if
  else
    $V_i(t) \leftarrow V_i(t) - 1$
  end if
  if $V_i(t) = 0$ **then**
    $S_i^{t+1} = S_i^t$
    $k = 1$
  end if
end while

3.1.3.2 Algorithm for the entire simulation

Algorithm 5 shows the algorithm for the entire simulation. First, we defined space of the corridor and the static field. Next, pedestrians were randomly placed in areas α and area β at $t = 0$ and the time step was initialized as $t = 0$. Afterwards, all the pedestrians were updated at each time step and moved until t_{MAX}. We set $t_{MAX} = 200$.

We adopted the ordered sequential procedure in this chapter, as in Chapter 2; namely, that pedestrians were updated from the right to the left. First, pedestrians who were in cell (x_{MAX}, y) were updated ($x_{MAX} = 798$). Subsequently, pedestrians who were in cell $(x_{MAX} - 1, y)$ were updated. In this way, the update of pedestrians was continued until $x = 0$ in each time step. In the case of multiple people in places in which the value of x was the same, the moving procedure was randomly updated among them. Note that collisions did not occur because of the sequential update.

3.2 Results

3.2.1 States in the corridor

Figure 3.6 illustrates a state of pedestrians in unidirectional flow in a corridor. The red cells denote pedestrians. The blue cells are the pedestrians' personal spaces and headways. The yellow cells express empty spaces and the black cells are the walls. The pedestrians moved in the direction of the pointed part of their personal space while keeping a distance in a direction to their movement in the corridor.

3.2.2 Relation between velocity profile and the form of static floor field

Figure 3.7(A) and (B) show the calculation results of the velocity profile for patterns A, B, C, and D. The flow state was not stable at the beginning of the simulation. We calculated the average speeds during the period where the flow state was sufficiently developed (i.e. the period where a steady-flow movement was attained). Figure 3.7(A) demonstrates the average speeds in each place against location y in area α calculated during the time period from $t = 101$ to 200. We set

Algorithm 5 Entire algorithm for movement

Require:

i: a pedestrian in corridor
t: time step
t_{MAX}: maximum value of time step
S_i^t: static floor field of pedestrian i at t
x: coordinate of the direction of the length of the corridor
x_{MAX}: maximum value of x
y: coordinate of the direction of the width of the corridor
cell (x, y): coordinates in corridor

Ensure: : Move pedestrians until t_{MAX}

Define space
Define static floor field
Place pedestrians in space randomly in area α and area β
$t \leftarrow 0$
while $(t < t_{MAX})$ **do**
  $x \leftarrow x_{MAX}$
  while $(x > 0)$ **do**
    for all i such that $S_i^t = x$ **do**
      Execute Algorithm 4
    end for
    $x \leftarrow x - 1$
  end while
  $t \leftarrow t + 1$
end while

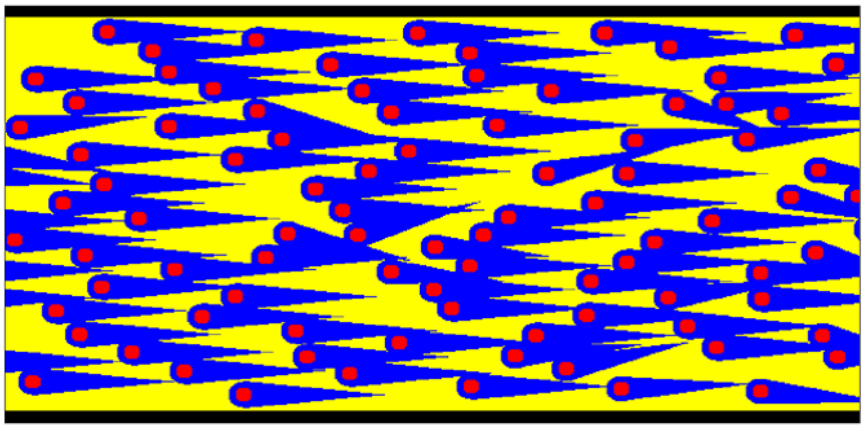

Figure 3.6: Schematic illustration of the unidirectional pedestrian flow in area α, where $\rho = 0.5$ pedestrians/m^2. The red, blue, yellow, and black cells are pedestrians, pedestrians' personal spaces and headways, empty spaces, and walls, respectively.

the initial density in the corridor for a comparison with experimental results [13], that is, the population density was 1.6 pedestrians/m^2 (352 pedestrians). We divided area α into 30 cm wide strips running parallel to the walls except a 50 cm wide strip near each wall. In each 30 cm wide strip, the average speeds were calculated from the speeds of pedestrians in each strip. Figure 3.7(B) presents the average densities against location y in area α from $t = 101$ to 200. We calculated the average densities by counting the number of the pedestrians. The average densities were calculated by the population in each strip during the given time. The average densities and speeds depended on the strip width. The variation in the average speeds and the population densities caused by varying the strip width was so small that the difference in values did not affect this discussion. As shown in Figure 3.7(A) and (B), the average speeds and densities did not depend on the strip in pattern A. The average speeds decreased and the average densities increased with decreasing proximity to the walls in pattern B, C, and D. Therefore, the intentions in space affected the velocity and density profiles. The results in pattern C, in particular, depicted a parabolic curve that is similar to experimental results [13].

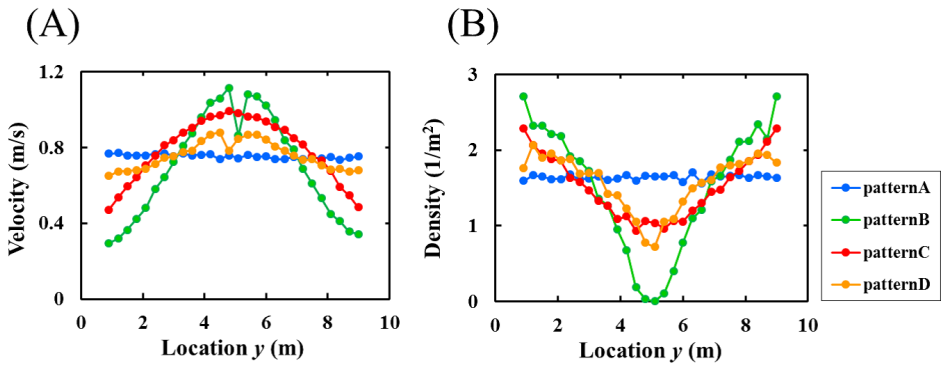

Figure 3.7: Calculation results of patterns A, B, C, and D, where $\rho = 1.6$ pedestrians/m^2. (A) Average speeds against location y. (B) Average densities against location y.

Figure 3.8(A), (B), and (C) show a comparison of the results changing the incline a in pattern C with previous experimental results [13]. We present the average speeds against location y in Figure 3.8(A), average densities against location y

in Figure 3.8(B), and flow rate against location y in Figure 3.8(C). Figure 3.8(A) and (B) depict the characteristics of our results qualitatively corresponding to previous results [13] in terms of the graph configuration. The parabolic curve was more moderate as the incline a decreased. Figure 3.8(C) shows that our results for the flow rates tended to be closer to the fixed value found in previous studies. From Figure 3.8(A) and (B), the incline $a = 0.5$ generates the results most similar to the previous experimental results [13].

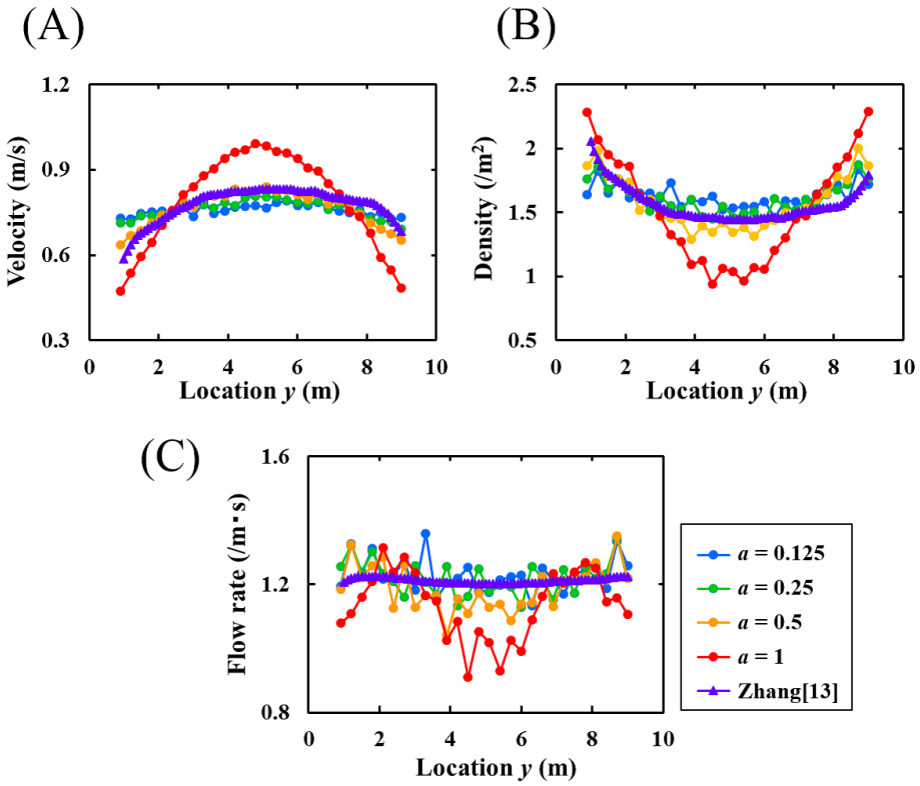

Figure 3.8: Calculation results in the case of changing a, where $\rho = 1.6$ pedestrians/m^2. (A) Average speeds against location y. (B) Average densities against location y. (C) Flow rate against location y. Note that the results of $a = 1$ are equal to those of pattern C in Figure 3.7.

Figure 3.9(A) and (B) show the relation between the average speeds and location y and the relation between the average densities and location y, respectively. From Figure 3.9(A) and (B), the results qualitatively agree with the previous

experimental results [13]. The average speeds in Figure 3.9(A), however, are faster than results integrating personal space and headway into pedestrians and experimental results in Figure 3.8(A).

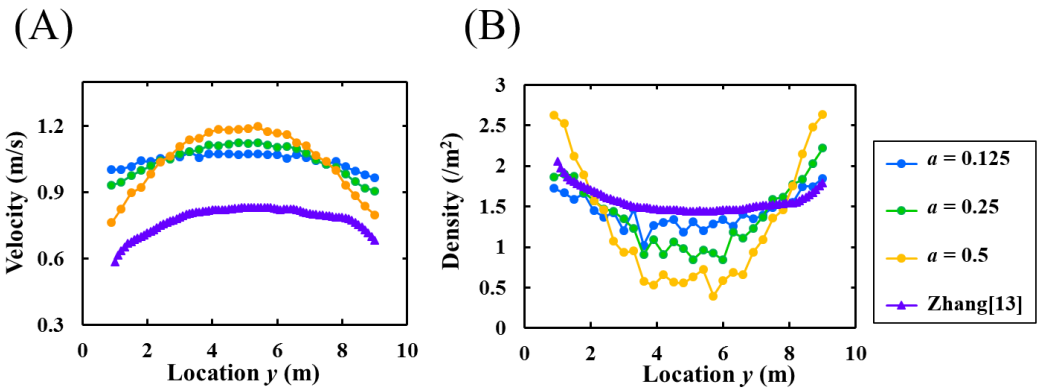

Figure 3.9: Calculation results without setting personal space and headway in the case of changing a, where $\rho = 1.6$ pedestrians/m^2. (A) Relation between average speeds and location y. (B) Relation between average densities and location y.

3.2.3 Case of changing body cell size

We investigated herein the case of changing body cell size, where the incline $a = 0.5$. Figure 3.10(A) depicts the relation between the average velocities and location y in the corridor. Figure 3.10(B) shows the relation between the average densities and location y. We used the initial parameters for each case of the cell size listed in Table 3.1. We used an Apple iMac with an Intel® Core i5 3.1 GHz processor and 4 GB 1,333 MHz DDR3 RAM. The figures show that the results are closer to the previous experimental results [13] as the cell size decreases, except for the case where the cell size is 1. Figure 3.10(C) shows each ratio of the calculation time for an 8 cm cell size to that of the other cases on a log–log graph. The calculation time per time step in the case of the 8 cm cell size was 7.09 seconds, which changed exponentially depending on the cell size.

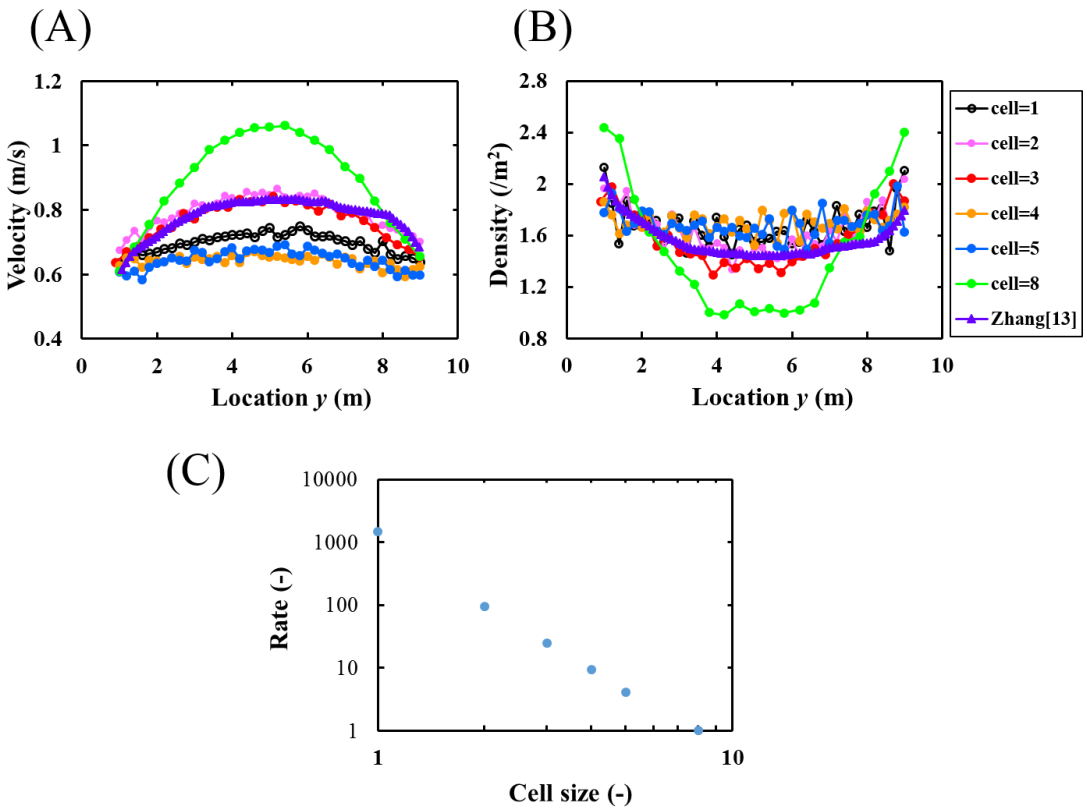

Figure 3.10: Calculation results in the case of changing the cell size from 1 to 8 cm, where $a = 0.5$ and $\rho = 1.6$. Note that the results of $a = 1$ are equal to those of pattern C in Figure 3.9. (A) Average speeds against location y. (B) Average densities against location y. (C) Log–log graph of the ratios of the calculation time for a cell size of 8 cm to that of the other cases.

3.2.4 Case of changing the population density

We analyzed herein the case of changing the initial population density ρ in pattern C. Figure 3.11(A) shows relations between the average velocities and the initial population densities in the corridor from $\rho = 0.5$ to $\rho = 3.0$ (pedestrians/m^2). The parabolic curve became more moderate as ρ increased. We showed the average speeds in area α against the population densities and the experimental data from Zhang et al. [16] (purple triangles), Weidmann [2] (green rhombuses), Seyfried et al. [3] (black dots), Helbing et al. [10] (closed circles), Mori and Tsuk-

aguchi [9] (orange crosses), Hankin and Wright [7] (pink crosses), and Polus et al. [8] (blue squares) and our results in pattern C in Figure 3.11(B). Figure 3.11(C) shows the relation between the population densities and the flow rates. The results in Figure 3.11(C) reproduced the nonlinear traffic characteristic that the flow rates gradually increased with the densities and decreased when the density was higher than a critical value. Our results showed a deadlock of pedestrians above approximately 3 pedestrians/m^2.

Table 3.1: Parameters and calculation time per time step in the case of changing cell size.

Cell size (cm)	Personal space (cm)	Body size (cm)	Calculation time (s)
1	15	39	1.05×10^4
2	14	38	6.68×10^2
3	15	39	1.76×10^2
4	16	36	6.60×10
8	16	40	7.09

Figure 3.12 presents the states of the stop-and-go wave in the corridor, where $\rho = 0.28$. The space in the corridor was divided into strips with a width of 10 cm each, vertically to the wall in the x-direction. The average velocities in each strip were then calculated. The average speeds became larger as the colors of the areas changed from red to yellow. The red areas express the stop state, where the average velocity was zero. The results demonstrated that the cluster of the stop state moved in a direction opposite to the movement of the pedestrians. That is, the stop-and-go waves happened in the corridor.

Figure 3.13 illustrates the relation between the population densities in the corridor and the ratios of the calculation time. The calculation time per time step increased as the density became larger because further calculation time was required to decide on the speed and direction of each pedestrian when the population density was large.

3.3 Discussion

As shown in Figure 3.5, we set four patterns of static floor field. Consequently, in the four patterns, the results of pattern C in Figure 3.7 most closely repro-

duced the experimental results in [13]. This is because pattern A did not indicate pedestrians' intention toward the wall. In patterns B and D, pedestrians attempted to go toward the wall even if they were on the center of the corridor. Therefore, average densities of the center decreased dramatically as shown in Figure 3.7(B). Meanwhile, in pattern C, the velocity profile and density profile depicted a parabolic curve because pedestrians who were located in the center of the corridor did not have strong intentions toward the wall.

We integrated personal space and headway into our simulation for more realistic assumptions. In fact, the results in Figure 3.8 were slower than the results that did not integrate personal space and headway in Figure 3.9 and could reproduce the previous experimental results [13]. We can say that pedestrians' speeds are controlled by integrating personal space and headway. Therefore, by integrating personal space and headway into the simulation, we could reproduce the more realistic results compared with the results that did not integrate personal space and headway. In conventional CA models and the other multi-grid methods [20, 25–27, 37–55], personal space and headway were not integrated into the models. In general, CA models have a disadvantage in terms of the quantitative reproduction of pedestrian dynamics. As indicated by our results, we have shown that integrating personal space and headway is a useful method for reproducing realistic results.

In Figure 3.11(B) and (C), there was a deadlock of pedestrians above approximately 3 pedestrians/m^2, although there are often real situations in which the density is greater than 3 pedestrians/m^2 [2, 7, 9, 10, 16]. This is because we set a strict rule by which a pedestrian walks, such that their personal space does not enter that of the other pedestrians. Meanwhile, as shown in Figure 3.11(B) and (C), the average speeds and flow rate agreed with several experimental results when the density is lower than 2.5 pedestrians/m^2. Therefore, our method is excellent at reproducing unidirectional pedestrian flow in a corridor except for the case of extremely large population density.

We could reproduce the pedestrian dynamics phenomenon similar to the Hagen–Poiseuille flow [74], a term used in fluid dynamics. This may mean that the pedestrian velocity profile can be represented using the fluid dynamics theory. Previous research [73], however, has shown that crowd motions must be treated as a free particle flow, not as a continuum flow. Other research [71] has implied that the

velocity profile was flat and the flow dependence on the street diameter did not obey the so-called Hagen–Poiseuille flow. In other words, the unique velocity profile of [13, 16], as with the Hagen–Poiseuille flow, was not generally formed in pedestrian dynamics. Thus, several conditions of population density and space characteristics for the parabolic curve of pedestrians' velocity profile may exist. If the underlying mechanism is understood, it will be possible to predict the danger zones of high-population-density spaces in the future.

3.4 Conclusions

We have focused on unidirectional pedestrian flow in a corridor to reproduce the velocity profiles observed in previous experiments [13, 16] using our simulation methods. To reproduce the experimental results, we hypothesized that pedestrians attempted to walk along the wall side as much as possible. To express the hypothesis, we set a CA model with the multi-grid and static floor field methods and calculated the velocity profiles and density profiles in our simulation. From the results, we confirmed that simulation results reproduced the experimental results in the case that the intentions of the pedestrians increased as they approached a wall. Therefore, our hypothesis that pedestrians attempt to walk along the wall side as much as possible was correct. We showed that simulations incorporating personal space and headway were more reproducible than simulations without integrating these parameters.

In the next chapter, we deal with traffic in a network to investigate the dynamics of traffic congestion in a space connecting roads focused on Chapter 3. We set a road-like network and examine the congestion movement. Based on the results, we qualitatively discuss the congestion movement. We also qualitatively discuss the difference between when the congestion occurs and when it does not.

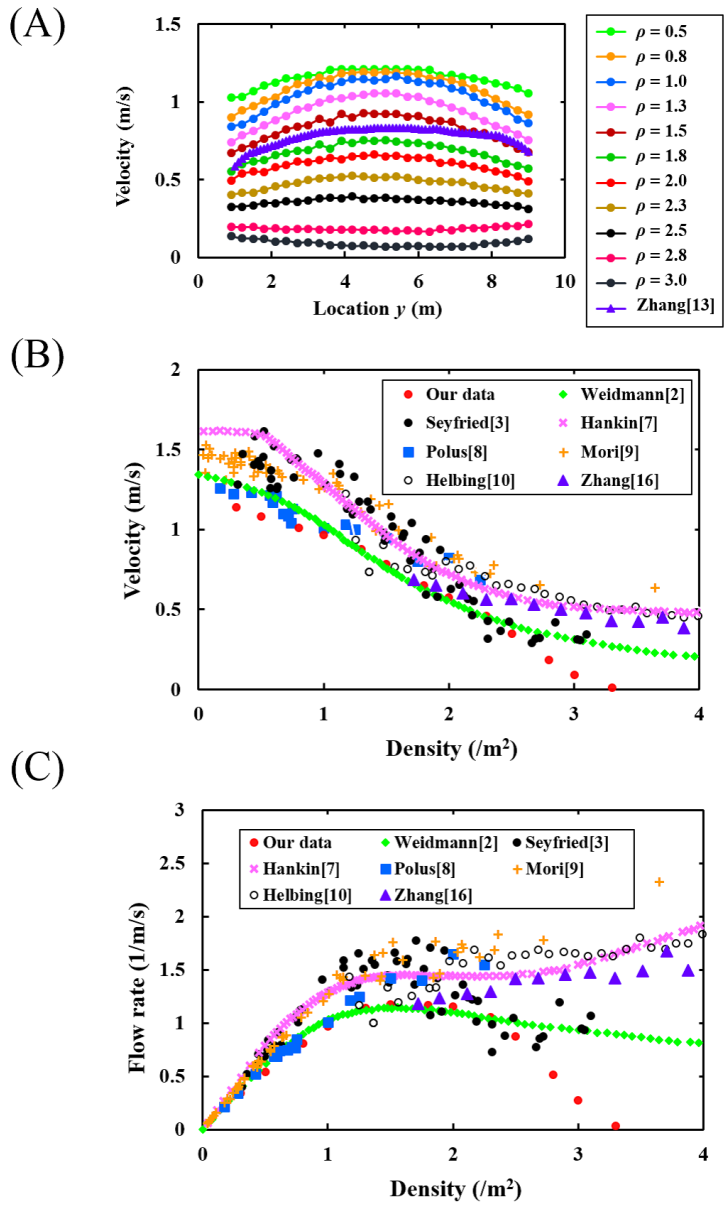

Figure 3.11: (A) Average speeds against location y in the case of changing ρ from 0.5 to 3, where $a = 0.5$, $V_{ideal} = 4.32$ km/h, and the experimental results from Zhang et al. [13]. (B) Average speeds against the population density and the data from Zhang et al. [16] (purple triangles), Weidmann [2] (green rhombuses), Seyfried et al. [3] (black dots), Helbing et al. [10] (closed circles), Mori and Tsukaguchi [9] (orange crosses), Hankin and Wright [7] (pink crosses), and Polus et al. [8] (blue squares) and our results in Pattern C. (C) Relation between the population densities and the flow rates in our data. Each data point corresponds to Figure 3.12(B)

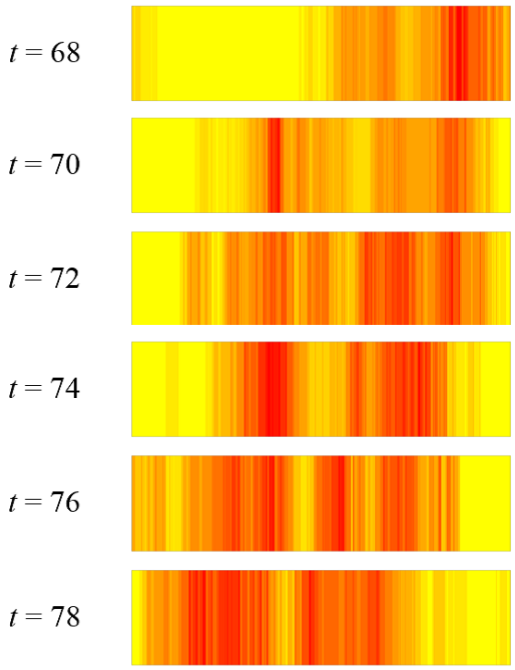

Figure 3.12: States of the stop-and-go wave in the corridor, where $\rho = 0.28$ from $t = 68$ to 78. The average speeds become larger as the colors of the areas change from red to yellow.

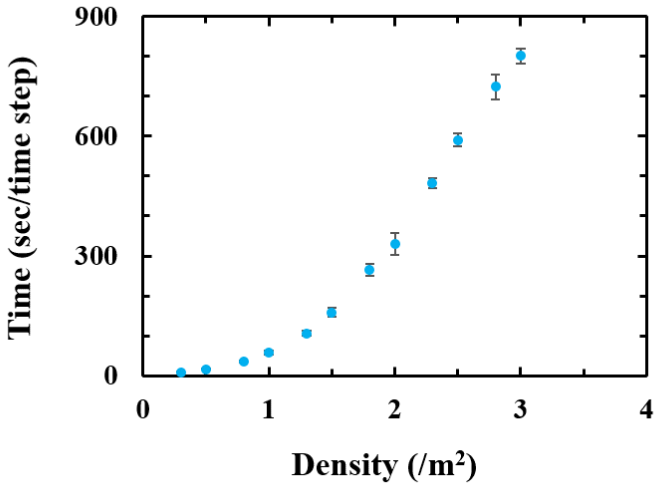

Figure 3.13: Relation between population densities in the corridor and ratios of the calculation time per one time step.

Chapter 4

Simulation and theorization of diffusion and disappearance of traffic congestion

In the previous chapter, we focused on the unidirectional flow in a corridor to reproduce experimental results [13, 16] and presented our hypothesis that pedestrians attempt to walk along the wall side as much as possible. In this chapter, we investigate the traffic dynamics of a multi-system connected roads assumed in Chapter 3, namely, consider the traffic dynamics more comprehensively. We focus on the dynamics of traffic congestion in a network. In a road-like network that connects multiple roads to each other, simulations are conducted to examine how the congestion propagates and subsequently resolves in the network. We improve the structure of the graph used in the density-control method [66] for a more realistic assumption. We set the traffic nonlinear characteristic in the model as shown in Figure 3.11(c) in Chapter 3. In the network, we first set a steady state and intentionally generate a traffic jam in an arc to observe how the state changes in the network. From the results, we confirm how the congestion moves and qualitatively analyze the condition when the traffic congestion resolves in the network. We compare the theoretical values with the simulation results in the phase diagram. We discuss the difference between our results and the previous results [66] and the usefulness of the method.

This chapter is organized as follows: Section 4.2 describes the graph and the simulation method used in this chapter; Section 4.3 presents the simulation

results and interprets them to qualitatively explain how the traffic jam spreads and determine the situations in which traffic congestion vanishes from the graph; and Section 4.4 presents conclusions.

4.1 Methods

4.1.1 Definition of the graph

We used the density-control method of [66], but the graph defined in this section was different from the graph in [66], where every vertex was assumed to include densities, rather than every arc. They also discussed the interaction among vertices. We assumed herein that densities existed in each arc for more realistic situations, where vehicles or pedestrians move in the network.

In our simulation, a cubic directed closed graph was assumed although a 10-regular directed closed graph was used in previous research [66]. This is because, for example, when we drive on a road and enter an intersection, we often choose from three directions: turn left, turn right, or go straight. Let us consider a digraph G consisting of a set V of vertices and a set A of arcs ($A \subset V \times V$). All in- and out-degrees in G had the same value (i.e. three), as shown in Figure 4.1(a). Note that a vertex and an arc represented a crossing and a one-way street, respectively. The number of vertices $|G|$ was 200 and arcs $\|G\|$ was 600. We drew 10 vertices vertically and 30 vertices horizontally to clearly visualize the state in G as shown in Figure 4.1(b). Each vertex was connected by arcs to the three neighboring vertices on the right. The rightmost vertices were joined to the three leftmost ones. The uppermost vertices were joined to the lowermost ones. Therefore, the structure of G was a torus. Here a_{ij} denotes an arc connecting vertex i to vertex j ($i \neq j \mid i, j \in V$) and l_{ij} denotes the length of a_{ij}.

4.1.2 Definition of the transportation rule

Each arc can include any number of objects that is a continuous value. The objects in each arc moved in the direction of the arc during each time step t. Here t was updated to $t + dt$. The density of the objects in a_{ij} at time t was denoted by ρ_{ij}. We use $F_{ij}(t)$ to denote the outflow from a_{ij} ($0 \leq F_{ij}(t) \leq 1$). The rules of inflows and outflows were as follows.

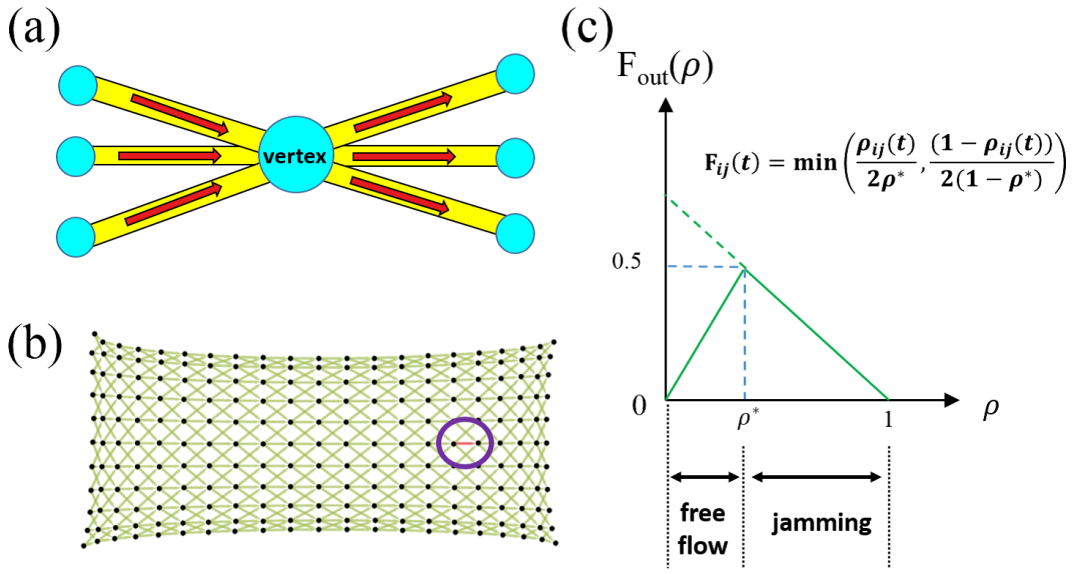

Figure 4.1: (a) Vertex with three arcs connected from and three arcs connected to other vertices. (b) Developed elevation of G. The uppermost vertices are identified with the lowermost vertices. In the same manner, the rightmost vertices are identified with the leftmost vertices. Therefore, the structure of G is a torus, and the objects move from the left to the right. In this simulation, we intentionally generate a traffic jam in an arc surrounded by the purple circle (i.e. red arc). (c) Equation (4.1) $F_{ij}(\rho)$ versus the density ρ.

i) The transportation flow decreased when the density exceeded a critical value as shown in Figure 3.11(C). The value of $F_{ij}(t)$ was determined as follows:

$$F_{ij}(t) = \min\left\{\frac{\rho_{ij}(t)}{2\rho^*}, \frac{1-\rho_{ij}(t)}{2(1-\rho^*)}\right\}, \tag{4.1}$$

where Equation (4.1) expressed the free-flow and jammed states as shown in Figure 4.1(c). Vehicles or pedestrians can generally move efficiently in the free-flow state. In contrast, the traffic flow in a jammed state gradually becomes inefficient and traffic congestion will possibly occur.

ii) The threshold ρ_{cl} was defined as a type of saturated density in the traffic flow. When the density in an arc exceeded ρ_{cl}, inflow into the arc was

prevented by closing its entrance and only outflow from the arc was allowed. A closed arc was opened when the density of the arc fell below ρ_{op} by discharging the density into another arc.

iii) As an inflow rule, a detouring pattern was adopted. In the pattern, the objects flowing from the outflow arcs were equally distributed to the inflow arcs. When an arrival arc was closed, the discharged objects from the departure arcs were distributed to the other arc, which was not closed. The outflow from the arc was cancelled if both destination arcs were closed. The time development of the density on the arc a_{ij} at time $(t + dt)$ was given as follows:

$$\begin{aligned} \frac{d\rho_{ij}(t)}{dt} &= \frac{P_{ij}(t) - Q_{ij}(t)}{l_{ij}} \\ &= \frac{1}{n}\sum_{h}^{V} \frac{B_{hi}C_{ij}(t)F_{hi}(t)}{l_{ij}} - \frac{1}{n}\sum_{k}^{V} \frac{B_{jk}C_{jk}(t)F_{ij}(t)}{l_{ij}}, \end{aligned} \quad (4.2)$$

where $P_{ij}(t)$ was the total inflow to a_{ij} at t, and $Q_{ij}(t)$ was the outflow from a_{ij} at t. Here B_{ij} was 1 when an arc a_{ij} $(i \neq j)$ existed; otherwise, B_{ij} was 0. $C_{ij}(t)$ was 1 or 0 if a_{ij} was opened or closed at t, respectively. In this simulation, a cubic graph was assumed, thus, $n = 3$.

4.1.3 Algorithm and parameter setting

Algorithm 6 shows the entire algorithm in this simulation. First, the vertices and the arcs in G were defined, after which the initial density $\overline{\rho}$ in each arc was set at $t = 0$ (i.e. the initial flow in G was in a steady state). Then, the density in an arc located on the right center in G as shown in Figure 4.1(b) was set as ρ_{cl} and the state of the arc was closed. Thereby, traffic congestion was intentionally generated to analyze its effect on the surrounding arcs. Afterwards, the density in each arc was calculated according to Equation (4.2). The density in each arc was updated after this calculation. Then t was updated to $(t + dt)$ and this was conducted until $t = t_{MAX}$. In this simulation, we set $dt = 0.0001$, $t_{MAX} = 100$, $\rho_{cl} = 0.75$, and $\rho^* = 0.5$.

Algorithm 6 Entire algorithm of the density-control method

Require:

t: time step
dt: each unit of time
t_{MAX}: maximum value of time step
a_{ij}: arc connecting from vertex i to vertex j
B_{ij}: adjacent matrix
$B_{ij} = 1$ if a_{ij} exist; otherwise, $B_{ij} = 0$.
C_{ij}: matrix expressing the open or closed state
$C_{ij} = 1$ if a_{ij} is opened; otherwise, $C_{ij} = 0$.
$\rho_{ij}(t)$: density in a_{ij} at t
ρ_{cl}: closure density
ρ_{op}: opened density
$\overline{\rho}$: average density

Ensure: : Conduct simulation until t_{MAX}

Define a_{ij} and, then, set $B_{ij} = 1$
Define a graph and adjacent matrix
for all a_{ij} such that $B_{ij} = 1$ **do**
  set $C_{ij} = 1$ and $\rho_{ij}(t) = \overline{\rho}$
end for
$t \leftarrow 0$
$\rho_{ij}(t) = \rho_{cl}$ and $C_{ij} = 0$ in an arc a_{ij}
Congestion occurs in the arc
while $(t < t_{MAX})$ **do**
  for all a_{ij} such that $B_{ij} = 1$ **do**
    Calculate $\frac{d\rho_{ij}(t)}{dt}$ according to Equation (4.2)
  end for
  for all a_{ij} such that $B_{ij} = 1$ **do**
    $\rho_{ij}(t + dt) = \rho_{ij}(t) + \frac{d\rho_{ij}(t)}{dt}$
    if $\rho_{ij}(t + dt) \geq \rho_{cl}$ **then**
      $C_{ij} = 0$
      Change from open state to closed state
    end if
    if $C_{ij} = 0$ and $\rho_{ij}(t + dt) \leq \rho_{op}$ **then**
      $C_{ij} = 1$
      Change from closed state to open state
    end if
  end for
  $t \leftarrow t + dt$
end while

4.2 Results

4.2.1 State of the graph after traffic congestion occurs

In the state of G at $t = 100$ and $\rho_{op} = 0.60$, there are three phases, the free-flow, the controlled, and the deadlock phases, as shown in Figure 4.2. These phases were obtained by changing $\overline{\rho}$. Note that the red arcs in Figure 4.2 express the congestion state. The traffic congestion in the free-flow state was solved immediately, and the state in G returned to the original steady state as shown in Figure 4.2(a). In the case of the controlled phase, some congestion continued to exist locally in G as shown in Figure 4.2(b). In contrast, all arcs in G in the deadlock phase were closed, and the flow in G broke down because of the congestion generated at $t = 0$ as shown in Figure 4.2(c).

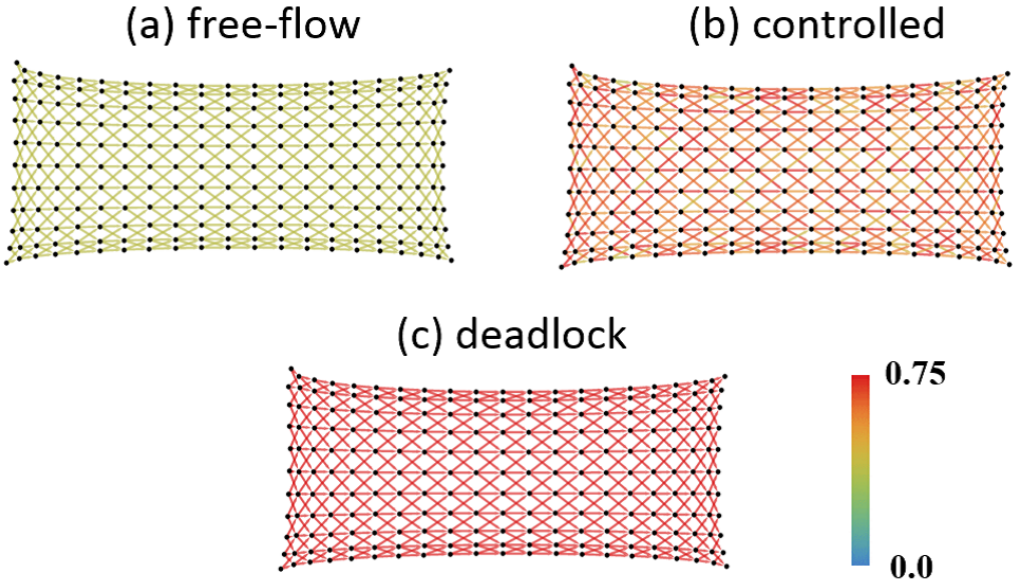

Figure 4.2: States in the graph in the free-flow, controlled, and deadlock phases, where $\rho_{op} = 0.60$ at $t = 100$, (a) $\overline{\rho} = 0.35$, (b) $\overline{\rho} = 0.60$, and (c) $\overline{\rho} = 0.75$. The value of the density matches the color bar.

Figure 4.3(a) shows the phase diagram in the $\overline{\rho}$ and ρ_{op} plane at $t = 100$. The phase depended on $\overline{\rho}$ and ρ_{op}. The area $*$ in Figure 4.3(a) was a kind of controlled phase. In this area, only the arc, in which congestion was intentionally

generated, repeated closed and open states when ρ_{op} was relatively large. The flow was always inefficient even if the arc was open. Figure 4.3(b) shows the MFD which is the relation between $\overline{\rho}$ and the average flow rate $\overline{Q}$ in G. Here $\overline{Q}$ was determined as $\overline{Q} = \frac{\sum_i^V \sum_j^V B_{ij} Q_{ij}}{\|G\|}$. Figure 4.3(a) and (b) illustrate that an efficient flow was achieved in the free-flow state, and in the states where the average flow rate $\overline{Q}$ was the same as the value of Equation (4.1) under $\rho^* = \frac{1}{2}$. Here, $\overline{Q}$ decreased when the phase changed from the free-flow to the controlled phase and gradually decreased as $\overline{\rho}$ increased. Eventually, $\overline{Q}$ was 0 in the deadlock phase. Note that the flow rate in $*$ achieved an efficient flow because there was only one closed arc.

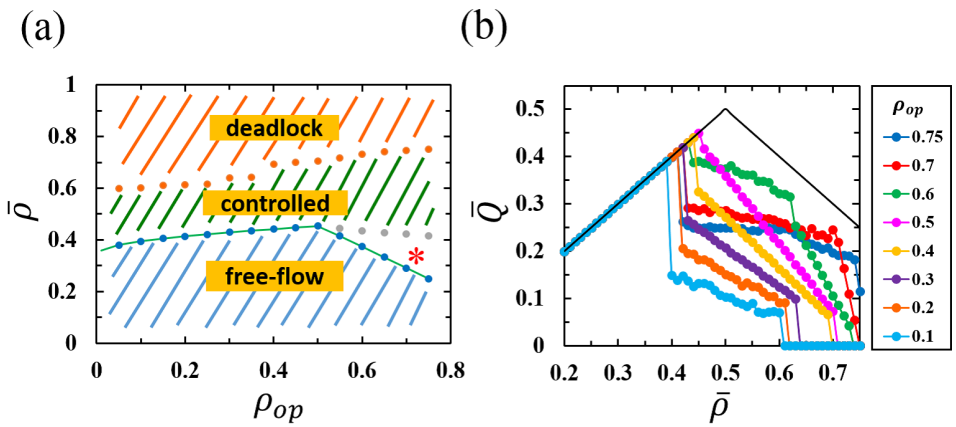

Figure 4.3: (a) Phase diagram for this simulation. The vertical and horizontal axes represent $\overline{\rho}$ and ρ_{op} at $t = 100$ and $\rho^* = 0.5$, respectively. The blue circles indicate the boundary between the free-flow and the controlled phases. The orange circles indicate the boundary between the controlled and the deadlock phases. The area with an asterisk surrounded by blue and gray circles shows the phase in which only the arc where the initial congestion has been intentionally generated repeats the steps from being in the closed state to the open state and vice versa. The green solid line is the theoretical value of Equation (4.8). (b) MFD of Figure 4.3(a). The vertical and horizontal axes denote $\overline{Q}$ and $\overline{\rho}$, respectively. The solid line corresponds to Equation (4.1) when $\rho^* = 0.5$.

4.2.2 How the traffic congestion spreads

The congestion dynamics in the controlled phase was analyzed in detail. In this phase, there were three congestion movement patterns: recession wave, stagnant, and traveling wave. These movements were observed by changing parameters ρ_{op} and $\overline{\rho}$. Figure 4.4 shows a snapshot of each movement pattern. In Figure 4.4(a), the congestion in the arc propagated in a direction opposite to the movement of the objects (to the left) as a recession wave. The width of the wave gradually increased, and the wave transformed into a large one. In Figure 4.4(b), the movement of the wave was similar to that of the wave in Figure 4.4(a) in the early stage. Meanwhile, the rear part of the congestion wave (right-hand side) was stagnant in several arcs. The speed of the top of the wave gradually decreased. In Figure 4.4(c), the congested arc affected not only the direction opposite to the movement of the objects, but also the direction of the movement of the objects (the traveling wave). After a while, the traveling wave collided with the recession wave, formed several new waves and moved towards the left of the graph. In Figure 4.4(d), the movement of the wave exhibited the same behavior as that in Figure 4.4(c) in an early stage. After that, however, the congestion wave did not grow, and each congestion wave continued to move finely in the graph. The phenomenon in Figure 4.4(a) and (b) was confirmed when $\overline{\rho}$ was less than 0.5, that is, $\overline{\rho}<\rho^*$; otherwise, the phenomenon shown in Figure 4.4(c) and (d) occurs. The simulation result shown in Figure 4.4(a) holds when ρ_{op} was relatively small. The result gradually had the nature of Figure 4.4(b) when ρ_{op} reached approximately 0.55 or more. In contrast, the phenomenon in Figure 4.4(c) began to move into that of Figure 4.4(d) when ρ_{op} reached approximately 0.58 or more. Both the recession and traveling waves propagated faster as the initial average density increased.

4.2.3 Kinds of situations in which the traffic congestion vanishes

The phase transition to determine whether a congested arc affects the arcs at the back (to the left in this simulation) was analyzed based on the theory shown in [66] when $\rho_{op} \leq \frac{1}{2}$ (or $\rho_{op} \leq \rho^*$). Let the critical density ρ' denote the density of the arcs next to the congested arc when the congested arc recovers from the closed state to the open state. That is, the congested arc affects the nearby arcs if the time $T_{\overline{\rho}\to\rho'}$, which is required for increasing the density of the arcs from $\overline{\rho}$

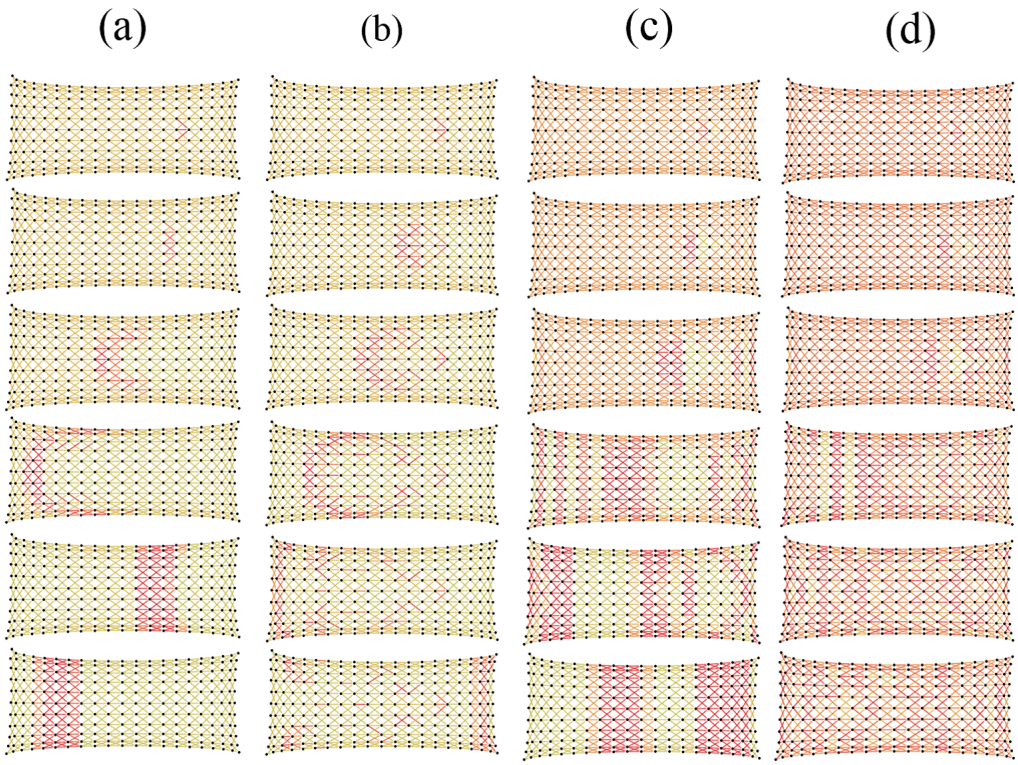

Figure 4.4: Snapshots of the wave propagation by the four patterns in the controlled phase. The conditions are as follows: (a) $\rho_{op} = 0.40$, $\overline{\rho} = 0.45$, at $t = 3$, 5, 10, 15, 25, and 45; (b) $\rho_{op} = 0.60$, $\overline{\rho} = 0.45$, at $t = 9$, 15, 20, 30, 40, and 50; (c) $\rho_{op} = 0.40$, $\overline{\rho} = 0.55$, at $t = 1$, 2, 3, 5, 10, and 20; and (d) $\rho_{op} = 0.60$, $\overline{\rho} = 0.60$, at $t = 1$, 2, 3, 5, 10, and 20.

to the critical density ρ', is larger than the time $T_{\rho_{cl} \to \rho_{op}}$ required to recover from the closed state to the open state. Equation (4.2) can be changed as $dt = \frac{d\rho}{-Q}$

(i.e. the normalization constant), then $T_{\rho_{cl}\to\rho_{op}}$ can be represented as

$$\begin{aligned} T_{\rho_{cl}\to\rho_{op}} &= \int_{\rho_{cl}}^{\rho_{op}} \frac{d\rho}{-Q} \\ &= \int_{\rho_{op}}^{\frac{1}{2}} \frac{d\rho}{\rho} + \int_{\frac{1}{2}}^{\rho_{cl}} \frac{d\rho}{1-\rho} \\ &= \log \frac{1}{4(1-\rho_{cl})\rho_{op}}. \end{aligned} \tag{4.3}$$

The congestion cluster does not propagate unless the inflow P in an arc is larger than the outflow Q on the road. Therefore, when $T_{\rho_{cl}\to\rho_{op}} = T_{\overline{\rho}\to\rho'}$, the boundary condition for whether a congested road affects the adjacent rear roads or not can be presented as follows:

$$\rho' = 1 - \overline{\rho}. \tag{4.4}$$

We assumed herein that the relation $\overline{\rho} < \frac{1}{2}$ always holds. Intuitively, this was true because of the simulation results in Figure 4.3(a). From Equation (4.2), assuming that the arc was in the steady state when $n = 3$, the time development of the density on an arc located on the back of the congested arc became

$$\begin{aligned} \frac{d\rho}{dt} &= P - Q \\ &= \overline{\rho} - \frac{2}{3}\min\{\rho, 1-\rho\}, \end{aligned} \tag{4.5}$$

where the inflow P is constant $\overline{\rho}$. Here $T_{\overline{\rho}\to\rho'}$ is given as follows when $\rho_{op} \leq \frac{1}{2}$:

$$\begin{aligned} T_{\overline{\rho}\to\rho'} &= \int_{\overline{\rho}}^{\rho'} \frac{d\rho}{Q_{in} - Q_{out}} \\ &= \int_{\overline{\rho}}^{\frac{1}{2}} \frac{d\rho}{\overline{\rho} - \frac{2}{3}\rho} + \int_{\frac{1}{2}}^{\rho'} \frac{d\rho}{\overline{\rho} - \frac{2}{3}(1-\rho)} \\ &= 2\int_{\overline{\rho}}^{\frac{1}{2}} \frac{d\rho}{\overline{\rho} - \frac{2}{3}\rho} \qquad (4.6) \\ &= 3\log\frac{\overline{\rho}}{3\overline{\rho} - 1}, \qquad (4.7) \end{aligned}$$

where Equation (4.6) is derived from the symmetry that $\rho' = 1 - \overline{\rho}$ as $\rho = \frac{1}{2}$ was regarded as a median. Assuming that the boundary density $\overline{\rho}_{trans}$ is the average density $\overline{\rho}$ when $T_{\overline{\rho}\to\rho'} = T_{\rho_{cl}\to\rho_{op}}$ and the boundary condition Equation (4.4), $\overline{\rho}_{trans}$ was derived from Equation (4.3) and Equation (4.7) as follows:

$$\overline{\rho}_{trans} = \frac{\left(\frac{1}{4(1-\rho_{cl})\rho_{op}}\right)^{\frac{1}{3}}}{3\left(\frac{1}{4(1-\rho_{cl})\rho_{op}}\right)^{\frac{1}{3}} - 1}. \qquad (4.8)$$

The theoretical values of Equation (4.8) matched the simulation results in Figure 4.3(a).

Here, Equation (4.8) was generalized. Equation (4.3) can be rewritten as follows when ρ^* is a variable (i.e. when F_{out} satisfies function (4.1)):

$$T_{\rho_{cl}\to\rho_{op}} = 2\log\left\{\left(\frac{\rho^*}{\rho_{op}}\right)^{\rho^*}\left(\frac{1-\rho^*}{1-\rho_{cl}}\right)^{(1-\rho^*)}\right\}. \qquad (4.9)$$

The boundary condition from Equation (4.4) was derived as follows:

$$\rho' = 1 - \frac{1-\rho^*}{\rho^*}\overline{\rho}. \qquad (4.10)$$

Assuming that the relations $\overline{\rho} < \rho^*$ and $P = \frac{\overline{\rho}}{2\rho^*}$ are always practical. When $\rho_{op} < \rho^*$, the following relation from Equation (4.5) and Equation (4.10) was derived:

$$\begin{aligned} T_{\overline{\rho}\to\rho'} &= \int_{\overline{\rho}}^{\rho^*} \frac{d\rho}{\frac{\overline{\rho}}{2\rho^*} - \frac{2}{3}\frac{\rho}{2\rho^*}} + \int_{\rho^*}^{\rho'} \frac{d\rho}{\frac{\overline{\rho}}{2\rho^*} - \frac{2}{3}\frac{1-\rho}{2(1-\rho^*)}} \\ &= 3\log\frac{\overline{\rho}}{3\overline{\rho} - 2\rho^*}. \end{aligned} \tag{4.11}$$

Finally, the following formula using Equation (4.9) and Equation (4.11) was obtained:

$$\overline{\rho}_{trans} = \frac{2\rho^* \left(\frac{\rho^*}{\rho_{op}}\right)^{\frac{2}{3}\rho^*} \left(\frac{1-\rho^*}{1-\rho_{cl}}\right)^{\frac{2}{3}(1-\rho^*)}}{3\left(\frac{\rho^*}{\rho_{op}}\right)^{\frac{2}{3}\rho^*} \left(\frac{1-\rho^*}{1-\rho_{cl}}\right)^{\frac{2}{3}(1-\rho^*)} - 1}. \tag{4.12}$$

Figure 4.5 shows the theoretical values of Equation (4.12) and the simulation results in each ρ^*, where $\rho_{cl} = 0.75$. The theoretical values matched the values from the simulation when $\rho_{op} \leq \rho^*$.

So far, the theoretical values were derived in the case of $n = 3$ in Equation (4.2). From the following, Equation (4.12) is further generalized and a theoretical formula without deciding the value of n is derived. That is, the time development of the density on an arc located on the back of the congested arc can allow Equation (4.5) to be rewritten as follows:

$$\begin{aligned} \frac{d\rho}{dt} &= P - Q \\ &= \overline{\rho} - \frac{n-1}{n}\min\{\rho, 1-\rho\}, \end{aligned} \tag{4.13}$$

From Equation (4.11), $T_{\overline{\rho}\to\rho'}$ in Equation (4.11) can be rewritten as

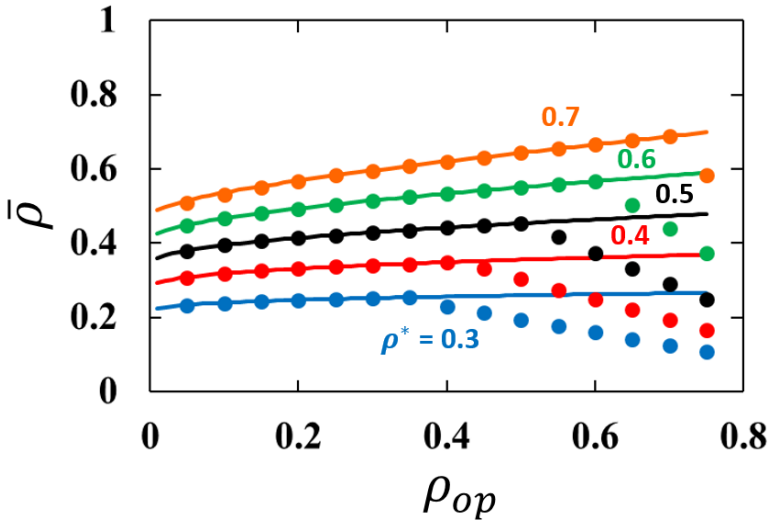

Figure 4.5: Contour lines between the free-flow and the controlled phases, where $\rho_{cl} = 0.75$. The solid lines express the theoretical values of Equation (4.12), whereas the dots express the simulation results, where $\rho_{cl} = 0.75$, ρ^* is 0.3 (blue), 0.4 (red), 0.5 (black), 0.6 (green), and 0.7 (orange). Note that the black dots and line in this figure correspond to the blue dots and blue line, respectively, in Figure 4.3(a).

$$T_{\bar{\rho}\to\rho'} = \int_{\bar{\rho}}^{\rho^*} \frac{d\rho}{\frac{\bar{\rho}}{2\rho^*} - \frac{n-1}{n}\frac{\rho}{2\rho^*}} + \int_{\rho^*}^{\rho'} \frac{d\rho}{\frac{\bar{\rho}}{2\rho^*} - \frac{n-1}{n}\frac{1-\rho}{2(1-\rho^*)}}$$

$$= \frac{2n}{n-1}\log\frac{\bar{\rho}}{n\bar{\rho} - (n-1)\rho^*}. \tag{4.14}$$

Finally, the following formula using Equation (4.9) and Equation (4.14) was derived:

$$\bar{\rho}_{trans} = \frac{(n-1)\rho^*\left(\frac{\rho^*}{\rho_{op}}\right)^{\frac{n-1}{n}\rho^*}\left(\frac{1-\rho^*}{1-\rho_{cl}}\right)^{\frac{n-1}{n}(1-\rho^*)}}{n\left(\frac{\rho^*}{\rho_{op}}\right)^{\frac{n-1}{n}\rho^*}\left(\frac{1-\rho^*}{1-\rho_{cl}}\right)^{\frac{n-1}{n}(1-\rho^*)} - 1}. \tag{4.15}$$

The theoretical values of Equation (4.15) are shown in Figure 4.6, where $\rho_{cl} = 0.75$, and (a) $\rho^* = 0.3$, (b) $\rho^* = 0.5$, and (c) $\rho^* = 0.7$. From the results, the area of free-flow state expands as n became larger.

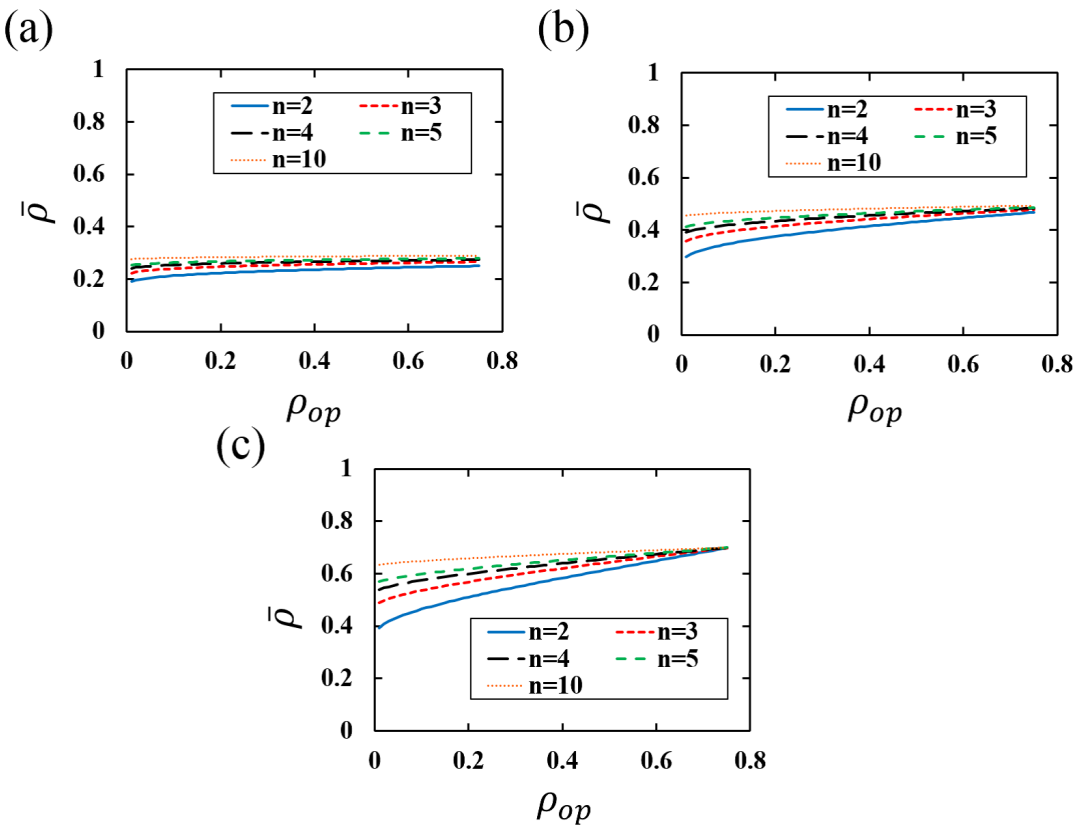

Figure 4.6: Contour lines between the free-flow and the controlled phases, where $\rho_{cl} = 0.75$ and (a) $\rho^* = 0.3$, (b) $\rho^* = 0.5$, and (c) $\rho^* = 0.7$, respectively. Each solid line when $n = 3$ in Figure 4.6 corresponds to each line in Figure 4.5.

4.3 Discussion

4.3.1 Mechanism of wave propagation

The mechanisms of three wave patterns (i.e. recession wave, stagnation wave, and traveling wave) were discussed in Section 4.2.2. First, the mechanism of a

recession wave, which was the congestion wave moving in a direction opposite to the movement of objects, was explained. Figure 4.7 shows a schematic illustration of a recession wave. When traffic congestion occurred in an arc (from vertex C to vertex A), the outflows from the two arcs (from vertex C to vertices B) located on the next congested arc decreased. Despite this, the inflow to these two arcs (from vertex C to vertices B) did not change. Hence, the density of these two arcs (from vertex C to vertices B) gradually increased. As a result, these two arcs (from vertex C to vertices B) fell into a state of congestion as well as the first congested arc (from vertex C to vertex A). Thereby, the outflows from the back of three arcs (from vertices E to vertex C) were stopped and the densities of these three arcs (from vertices E to vertex C) also fell into a state of congestion. This event successively propagated in a direction opposite to the movement as the recession wave (from vertices D to vertices E and then from vertices F to vertices D). The recession wave is similar to a stop-and-go wave in terms of the fact that both waves propagate in a direction opposite to the movement.

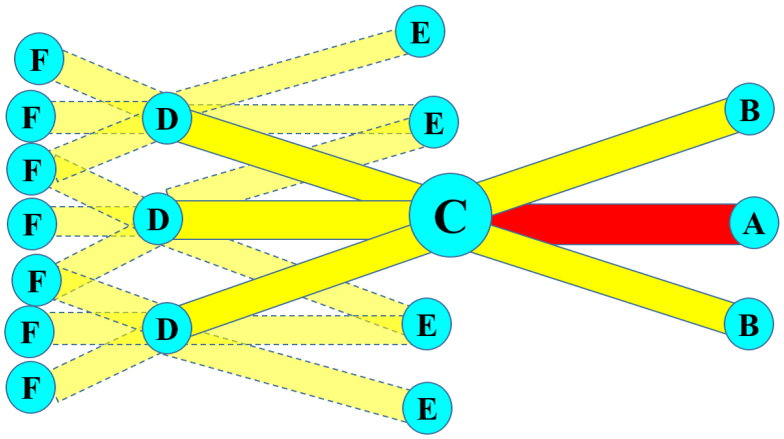

Figure 4.7: Schematic illustration of a recession wave.

In the case of a stagnation wave pattern, the congested arc had difficulty recovering from the jammed state to the free-flow state because the value of ρ_{op} was relatively large, and the flow became inefficient even if the arc returned from the closed state to the open state. Thus, the arc was no longer in the inefficient

flow state and alternated between the closed and the open states. The stagnation state may be observed in roads near a railroad crossing in a big city. This is because the railroad crossing will be closed soon even if the crossing is opened in the places where trains frequently pass. We can often observe roads that are always in a jammed state near the crossing.

The traveling wave occurred when $\overline{\rho}$ was relatively large, namely, $\overline{\rho}>\frac{1}{2}$ (more generally, $\overline{\rho}>\rho^*$). In this case, the recession wave also occurs at the same time. Figure 4.8 shows a schematic illustration of a traveling wave. In the traveling wave pattern, the outflow from the congested arc (from vertex A to vertex B) was smaller than the outflows from the three arcs (from vertex B to vertices C) located on the right-hand side of the congested arc (from vertex A to vertex B). Thereby, the densities in these three arcs (from vertex B to vertices C) gradually decreased, and the outflow from these arcs (from vertex B to vertices C) increased according to Equation (4.1). Afterwards, the inflows of arcs (from vertices C to vertices D) located on the right-hand side of the three arcs (from vertex B to vertices C) increased. Finally, these arcs (from vertices C to vertices D) changed from the inefficient flow state to the congestion state. The wave propagated to the right by repeating the mechanism in a direction to the right (from vertices C to vertices D and then from vertices D to vertices E). Intuitively, the traveling wave pattern may be an unrealistic phenomenon because, in principle, a pedestrian or a vehicle cannot affect others who exist in front of them.

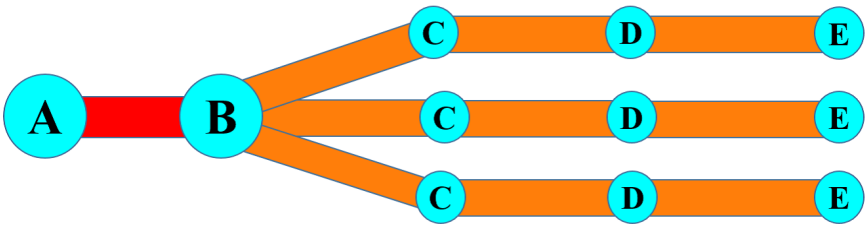

Figure 4.8: Schematic illustration of a traveling wave.

4.3.2 Comparison with the CA method

Figure 4.9 shows a relation between the densities in the network and the average calculation times per one time step by using an Apple iMac with an Intel® Core i5 3.1 GHz processor and 4 GB 1,333 MHz DDR3 RAM. The trials in each density were conducted 10 times, and the average times and variances were calculated. There were two qualitative differences between the results of Figs 3.13 and 4.9. First, the average calculation time did not depend on the density in Figure 4.9; in contrast, the calculation time in Figure 3.13 increased exponentially according to the density. Second, the calculation time of Figure 4.9 was much shorter than that of Figure 3.13. Therefore, the density-control method has an advantage in traffic network analysis in terms of calculation time. The density-control method, however, is unsuitable in the case that we reproduce the phenomenon such as in typical congestion in a corridor [13, 16]. Therefore, the density-control method is useful when we analyze the traffic dynamics more comprehensively.

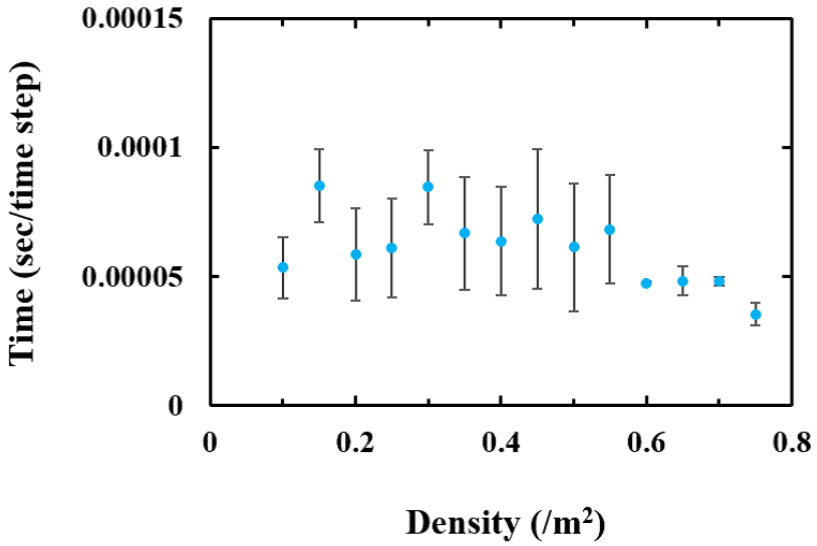

Figure 4.9: Relation between the average density in the network and the ratios of calculation time per one time step.

4.3.3 Phase diagram and generalization

As shown in Figure 4.2, we confirmed that there were three phases, free flow, controlled, and deadlock, as in the previous results [66]. However, the phase diagram in Figure 4.3(a) is a little different from the phase diagram in [66]. It is assumed that our initial condition of densities in each arc is different from that in [66]. We assumed the steady state as the initial congestion and intentionally generated a congestion in an arc. Meanwhile, they assigned the density value randomly in a certain range as the initial condition, namely, it was not steady state.

In previous research [66], They discussed the breakdown of a system in a transportation network, namely, the boundary condition between the controlled and deadlock in the phase diagram. In our simulation, meanwhile, we analyzed the boundary condition between the free-flow phase and the controlled phase. In Figure 4.6, as n was larger, $\overline{\rho}_{trans}$ becomes larger, that is, the area of the free-flow state was expanded. This means that the more the number of the adjacent arcs of an arc increases, the more the traffic congestion propagates to the adjacent arcs. This is because when the number of adjacent arcs is high, the burden of outflows per an arc is mitigated. The theory in Section 4.2.3 and the results of Figs 4.5 and 4.6 will aid in the realization of a road-network structure to achieve efficient traffic flow in a real-world network.

4.4 Conclusions

We have examined how the congestion propagates and resolves in the network. We used a density-control method and assumed a cubic directed closed graph that was a road-like network. In the network, we intentionally generated a traffic jam in an arc to analyze how the state changed in the network. From the results, we observed three congestion wave patterns: recession wave, stagnation wave, and traveling wave. We provided the condition when the traffic congestion resolves in the network and confirmed that the theoretical values partially corresponded to the simulation results. The density-control method is useful when we analyze the traffic dynamics more comprehensively.

Chapter 5

Conclusions

In this dissertation, we have studied dynamical traffic congestion in space such as room, corridor, and network using simulation methods. To analyze the dynamics in each system, we used a CA method in Chapters 2 and 3 and a density-control method in Chapter 4. We obtained knowledge about traffic dynamics in each chapter.

In Chapter 2, we dealt with the pedestrian dynamics in a room to examine the motion of pedestrians that leave a room. We set an improved CA model integrating the multi-grid method and the static floor field method. In the model, the form of pedestrians, their speed, their intentionality toward the exit, and the form of the room were defined in detail. The pedestrians were randomly located in a room and headed towards the exit. We investigated the relation between the time for completion of evacuation and the initial number of pedestrians in the room. From the results, we confirmed that there are three phases: large variance, stable, and linear. In the large variance phase, pedestrians moved straight toward the exit and rapid evacuations were achieved. The variance of the average time for completion of evacuation was large because the time for completion of evacuation depends on the distance of the farthest pedestrian from the exit. In stable phase, semi-circular congestion near the exit was formed. The time for completion of evacuation was only slightly dependent on the initial number of pedestrians in the room in this phase. Pedestrians in and around the congestion moved in a zig-zag course and detoured in the room. In the linear phase, though there was congestion near the exit in the stable phase as well, the time for completion of evacuation increased linearly according to the initial number of pedestrians. From

the results, we showed the usefulness of our model by comparing our results with results of a previous simulation model.

In Chapter 3, we focused on the unidirectional pedestrian flow in a corridor and the peculiar traffic phenomenon in a corridor. That is, the velocity profile in a corridor is a parabolic curve, in which the velocity was smaller as the wall of a corridor was approached. To reproduce the phenomenon, we hypothesized that pedestrians attempted to walk along the wall side as much as possible. To confirm whether the hypothesis is correct, we set the CA model with the multi-grid and static floor field methods, which can integrate personal space, headway, and intentionality toward the wall. Pedestrians moved in a corridor and velocity profiles were investigated. Then, we confirmed that the simulation results reproduced the data of observation under the hypothesis that the intentions of the pedestrians increase as they approached a wall.

In Chapter 4, we focused on the traffic dynamics in a network to examine how the congestion propagates and resolves in the network. We used a density-control method, and constructed a cubic directed closed graph such as a road network. We intentionally generated a traffic jam in an arc of the network under a steady state. We examined the states after the appearance of congestion, and observed three congestion wave patterns: recession wave, stagnation wave, and traveling wave. The recession wave was the wave that propagated in a direction opposite to the movement of the objects. In the stagnant pattern, several congestion waves remained in the same arc for a long time. The traveling wave which is propagating in the direction of movement of the objects was observed. We also theoretically evaluated the conditions when the traffic congestion resolves in the network, namely, the boundary conditions between free-flow and the controlled phases. As a result, the theoretical values partially corresponded to the simulation results.

Table 5.1 lists the differences of the movements of objects, which are caused depending on the objects such as pedestrians and vehicles and the space shapes such as room, corridor, and network, based on the results obtained in Chapters 2–4. That is, where traffic congestion occurred, how the congestion changed with time, and how the congestion resolved in a room, in a corridor, and in a network. We can regard a room and a corridor as in contrast to a network, which is a multi-system consisting of multiple roads. In a room, congestion happened near

an exit, formed a semi-circular shape, and remained near the exit. Then, the congestion was gradually cleared because the pedestrians who formed the jam left the room, and finally, the congestion resolved. In the case of a corridor, congestion happened near the wall sides of the corridor and remained in place. Furthermore, stop-and-go waves were observed when the density was extremely large and propagated in a direction opposite to the movement of pedestrians. In a network, we intentionally generated congestion on a road and observed three congestion wave patterns: recession wave, stagnation wave, and traveling wave. The cluster wave propagating in a direction opposite to the moving direction was observed in dynamics in unidirectional pedestrian flow and traffic flow in a road-like network. However, such a wave pattern was not observed in a room. The congestion existed in the corridor and in the network. This is because the structures of the simulation space were periodic.

Table 5.1: Characteristics of traffic congestion in each system.

	Room (Chapter 2)	Corridor (Chapter 3)	Network (Chapter 4)
subjects	pedestrians	pedestrians	pedestrians; vehicles
scale	subsystem	subsystem	multi-system
intention	toward exit	in one direction; toward wall	in one direction
location of congestion	near exit	near wall; on a road	on a road
propagation method	none	stay wall side; stop-and-go	recession; stagnation; traveling

We have clarified the differences of the movements of objects, which are caused depending on the objects such as pedestrians and vehicles and the space shapes such as room, corridor, and network for better understanding of the traffic dynamics. These results will contribute to resolve social problems such as traffic accidents, air pollution, and financial losses, caused by traffic congestion in urban areas. It will be possible to develop a time-dependent shortest path algo-

rithm [75–80] that can predict dynamical congestion and divert the congestion so that destinations can be reached more quickly.

Bibliography

[1] B. S. Kerner, H. Rehborn. Experimental properties of phase transitions in traffic flow. *Physical Review Letters*, 79(20):4030, 1997.

[2] U. Weidmann. Transporttechnik der Fussganger: Transporttechnische Eigenschaften des Fussgangerverkehrs. *Institute for Transport Planning and Systems*, Swiss Federal Institute of Technology, Swiss Federal Institute of Technology, Zurich, 1993.

[3] A. Seyfried, B. Steffen, W. Klingsch, and M. Boltes. The fundamental diagram of pedestrian movement revisited. *Journal of Statistical Mechanics: Theory and Experiment*, 2005(10):P10002, 2005.

[4] B. S. Kerner, H. Rehborn. Experimental properties of complexity in traffic flow. *Physical Review E*, 53(5):R4275, 1996.

[5] N. Geroliminis and C. F. Daganzo. Existence of urban-scale macroscopic fundamental diagrams: Some experimental findings. *Transportation Research Part B: Methodological*, 42(9):759-770, 2008.

[6] Y. Sugiyama, M. Fukui, M. Kikuchi, K. Hasebe, A. Nakayama, and K. Nishinari. Traffic jams without bottlenecks-experimental evidence for the physical mechanism of the formation of a jam. *New journal of physics*, 10.3: 033001, 2008.

[7] B. D. Hankin and R. A. Wright. Passenger flow in subways. *OR*, 9(2):81-88, 1958.

[8] A. Polus, J. Schofer, and A. Ushpiz. Pedestrian flow and level of service. *Journal of Transportation Engineering*, 109(1):46-56, 1983.

[9] M. Mori and H. Tsukaguchi. A new method for evaluation of level of service in pedestrian facilities. *Transportation Research Part A: General*, 21(3):223-234, 1987.

[10] D. Helbing, A. Johansson, and H. Z. Al-Abideen. Dynamics of crowd disasters: An empirical study. *Physical Review E*, 75(4):046109, 2007.

[11] V.V. Kholshevnikov, T. J. Shields, K. E. Boyce and D. A. Samoshin. Recent developments in pedestrian flow theory and research in Russia. *Fire Safety Journal*, 43(2):108-118, 2008.

[12] A. Jelic, C. Appert-Rolland, S. Lemercier, and J. Pettre. Properties of pedestrians walking in line: Fundamental diagrams. *Physical Review E*, 85(3):036111, 2012.

[13] X. L. Zhang, W. G. Weng, and H. Y. Yuan. Empirical study of crowd behavior during a real mass event. *Journal of Statistical Mechanics: Theory and Experiment*, 2012(08):P08012, 2012.

[14] B. S. Kerner. Experimental features of self-organization in traffic flow. *Physical Review Letters*, 81(17):3797, 1998.

[15] S. Tadaki, M. Kikuchi, A. Nakayama, A. Shibata, Y. Sugiyama, and S. Yukawa. Characterizing and distinguishing free and jammed traffic flows from the distribution and correlation of experimental speed data. *New Journal of Physics*, 18(8):083022, 2016.

[16] X. L. Zhang, W. G. Weng, H. Y. Yuan, and J. G. Chen. Empirical study of a unidirectional dense crowd during a real mass event. *Physica A: Statistical Mechanics and its Applications*, 392(12):2781-2791, 2013.

[17] B. Krausz and C. Bauckhage. Loveparade 2010: Automatic video analysis of a crowd disaster. *Computer Vision and Image Understanding*, 116(3):307-319, 2012.

[18] J.Y. Wang, W. G. Weng, and X. L. Zhang. New insights into the crowd characteristics in Mina. *Journal of Statistical Mechanics: Theory and Experiment*, 2014(11):P11003, 2014.

[19] A. Garcimartin, I. Zuriguel, J. M. Pastor, C. Martin-Gomez, and D. R. Parisi. Experimental evidence of the "Faster Is Slower" effect. *Proceedings of The Conference on Pedestrian and Evacuation Dynamics 2014*, 2:760-767, 2014.

[20] K. Shimura, K. Ohtsuka, G. Vizzari, and K. Nishinari. Mobility analysis of the aged pedestrians by experiment and simulation. *Pattern Recognition Letters*, 44:58-63, 2014.

[21] W. Song, W. Lv, and Z. Fang. Experiment and modeling of microscopic movement characteristic of pedestrians. *Proceedings of The 9th Asia-Oceania Symposium on Fire Science and Technology*, 62:56-70, 2013.

[22] D. Jezbera, D. Kordek, J. Kriz, P. Seba, and P. Sroll. Walkers on the circle. *Journal of Statistical Mechanics: Theory and Experiment*, 2010(01):L01001, 2010.

[23] M. Isobe, D. Helbing, and T. Nagatani. Experiment, theory, and simulation of the evacuation of a room without visibility. *Physical Review E*, 69(6):066132, 2004.

[24] T. Kretz, A. Grunebohm, and M. Schreckenberg. Experimental study of pedestrian flow through a bottleneck. *Journal of Statistical Mechanics: Theory and Experiment*, 2006(10):P10014, 2006.

[25] J. Zhang, W. Song, and X. Xu. Experiment and multi-grid modeling of evacuation from a classroom. *Physica A: Statistical Mechanics and its Applications*, 387(23):5901-5909, 2008.

[26] Z. Fang, W. Song, J. Zhang, and H. Wu. Experiment and modeling of exit-selecting behaviors during a building evacuation. *Physica A: Statistical Mechanics and its Applications*, 389(4):815-824, 2010.

[27] S. Cao, W. Song, W. Lv, and Z. Fang. A multi-grid model for pedestrian evacuation in a room without visibility. *Physica A: Statistical Mechanics and its Applications*, 436:45-61, 2015.

[28] M. Asano, T. Iryo, and M. Kuwahara. Microscopic pedestrian simulation model combined with a tactical model for route choice behaviour. *Transportation Research Part C: Emerging Technologies*, 18(6):842-855, 2010.

[29] M. Plaue, M. Chen, G. Barwolff, and H. Schwandt. Trajectory extraction and density analysis of intersecting pedestrian flows from video recordings. *Proceedings of Photogrammetric image analysis*, 285-296, Springer, Berlin, Heidelberg, 2011.

[30] L. Sun, L. Liu, Z. Xu, Y. Jie, D. Wei, and P. Wang. Locating inefficient links in a large-scale transportation network. *Physica A: Statistical Mechanics and is Applications*, 419:537-545, 2015.

[31] H. Nguyen, M. Liu, and F. Chen. Discovering congestion propagation patterns in spatio-temporal traffic data. *IEEE Transactions on Big Data*, 3(2):169-180, 2017.

[32] D. Helbing and P. Molnar. Social force model for pedestrian dynamics. *Physical review E*, 51(5):4282, 1995.

[33] D. Helbing, I. Farkas, and T. Vicsek. Simulating dynamical features of escape panic. *Nature*, 407:487-490, 2000.

[34] D. Helbing, I. J. Farkas, and T. Vicsek. Freezing by heating in a driven mesoscopic system. *Physical review letters*, 84(6):1240, 2000.

[35] L. Hou, J. G. Liu, X. Pan, and B. H. Wang. A social force evacuation model with the leadership effect. *Physica A: Statistical Mechanics and its Applications*, 400:93-99, 2014.

[36] K. Suzuno, A. Tomoeda, and D. Ueyama. Analytical investigation of the faster-is-slower effect with a simplified phenomenological model. *Physical Review E*, 88(5):052813, 2013.

[37] A. Kirchner, H. Klupfel, K. Nishinari, A. Schadschneider, and M. Schreckenberg. Simulation of competitive egress behavior: comparison with aircraft evacuation data. *Physica A: Statistical Mechanics and its Applications*, 324(3):689-697, 2003.

[38] Y. Weifeng and T. K. Hai. A novel algorithm of simulating multi-velocity evacuation based on cellular automata modeling and tenability condition. *Physica A: Statistical Mechanics and its Applications*, 379(1):250-262, 2007.

[39] S. Heliovaara, H. Ehtamo, D. Helbing, and T. Korhonen. Patient and impatient pedestrians in a spatial game for egress congestion. *Physical Review E*, 87(1):012802, 2013.

[40] X. Ji, X. Zhou, and B. Ran. A cell-based study on pedestrian acceleration and overtaking in a transfer station corridor. *Physica A: Statistical Mechanics and its Applications*, 392(8):1828-1839, 2013.

[41] A. Varas, M. D. Cornejo, D. Mainemer, B. Toledo, J. Rogan, V. Munoz, J. A. Valdivia. Cellular automaton model for evacuation process with obstacles. *Physica A: Statistical Mechanics and its Applications*, 382(2):631-642, 2007.

[42] K. Yamamoto, S, Kokubo, and K. Nishinari. Simulation for pedestrian dynamics by real-coded cellular automata (RCA). *Physica A: Statistical Mechanics and its Applications*, 379(2):654-660, 2007.

[43] X. Zheng, W. Li, and C. Guan. Simulation of evacuation processes in a square with a partition wall using a cellular automaton model for pedestrian dynamics. *Physica A: Statistical Mechanics and its Applications*, 389(11):2177-2188, 2010.

[44] Y. Suma, D. Yanagisawa, and K. Nishinari. Anticipation effect in pedestrian dynamics: Modeling and experiments. *Physica A: Statistical Mechanics and its Applications*, 391(1):248-263, 2012.

[45] Z. Fu, L. Yang, Y. Chen, K. Zhu, and S. Zhu. The effect of individual tendency on crowd evacuation efficiency under inhomogeneous exit attraction using a static field modified FFCA model. *Physica A: Statistical Mechanics and its Applications*, 392(23):6090-6099, 2013.

[46] X. Wei, W. Song, W. Lv, X. Liu, and L. Fu. Defining static floor field of evacuation model in large exit scenario. *Simulation Modelling Practice and Theory*, 40:122-131, 2014.

[47] T. Huan-Huan, D. Li-Yun, and X. Yu. Influence of the exits' configuration on evacuation process in a room without obstacle. *Physica A: Statistical Mechanics and its Applications*, 420:164-178, 2015.

[48] Z. Fu, X. Zhou, K. Zhu, Y. Chen, Y. Zhuang, Y. Hu, L. Yang, C. Chen, and J. Li. A floor field cellular automaton for crowd evacuation considering different walking abilities. *Physica A: Statistical Mechanics and its Applications*, 420:294-303, 2015.

[49] C. Burstedde, K. Klauck, A. Schadschneider, and J. Zottartz. Simulation of pedestrian dynamics using a two-dimensional cellular automaton. *Physica A: Statistical Mechanics and its Applications*, 295(3):507-525, 2001.

[50] A. Kirchner and A. Schadschneider. Simulation of evacuation processes using a bionics-inspired cellular automaton model for pedestrian dynamics. *Physica A: statistical mechanics and its applications*, 312(1):260-276, 2002.

[51] A. Kirchner, K. Nishinari, and A. Schadschneider. Friction effects and clogging in a cellular automaton model for pedestrian dynamics. *Physical review E*, 67(5):056122, 2003.

[52] R. Y. Guo, and H. J. Huang. A modified floor field cellular automata model for pedestrian evacuation simulation. *Journal of Physics A: Mathematical and Theoretical*, 41(38):385104, 2008.

[53] W. Guo, X. Wang, M. Liu, Y. Cheng, and X. Zheng. Modification of the dynamic floor field model by the heterogeneous bosons. *Physica A: Statistical Mechanics and its Applications*, 417:358-366, 2015.

[54] W. Song, X. Xu, B. H. Wang, and S. Ni. Simulation of evacuation processes using a multi-grid model for pedestrian dynamics. *Physica A: Statistical Mechanics and its Applications*, 363(2):492-500, 2006.

[55] W. G. Weng, L. L. Pan, S. F. Shen, and H. Y. Yuan. Small-grid analysis of discrete model for evacuation from a hall. *Physica A: Statistical Mechanics and its Applications*, 374(2):821-826, 2007.

[56] D. Helbing, M. Isobe, T. Nagatani, and K. Takimoto. Lattice gas simulation of experimentally studied evacuation dynamics. *Physical review E*, 67(6):067101, 2003.

[57] Y. Tajima and T. Nagatani. Scaling behavior of crowd flow outside a hall. *Physica A: Statistical Mechanics and its Applications*, 292(1):545-554, 2001.

[58] Y. Tajima, K. Takimoto, and T. Nagatani. Scaling of pedestrian channel flow with a bottleneck. *Physica A: Statistical Mechanics and its Applications*, 294(1):257-268, 2001.

[59] D. M. Shi and B. H. Wang. Evacuation of pedestrians from a single room by using snowdrift game theories. *Physical Review E*, 87(2):022802, 2013.

[60] J. Wu, X. Wang, J. Chen, G. Shu, and Y. Li. The position of a door can significantly impact on pedestrians' evacuation time in an emergency. *Applied Mathematics and Computation*, 258:29-35, 2015.

[61] R. M. Colombo and M. D. Rosini. Pedestrian flows and non-classical shocks. *Mathematical Methods in the Applied Sciences*, 28(13):1553-1567, 2005.

[62] I. Sivers and G. Koster. Dynamic stride length adaptation according to utility and personal space. *Transportation Research Part B: Methodological*, 74:104-117, 2015.

[63] C. F. Daganzo. The cell transmission model: A dynamic representation of highway traffic consistent with the hydrodynamic theory. *Transportation Research Part B: Methodological*, 28(4):269-287, 1994.

[64] R. Tao, Y. Xi, and D. Li. Simulation analysis on urban traffic congestion propagation based on complex network. In *Proceedings of the 2016 IEEE International Conference on Service Operations and Logistics, and Informatics (SOLI)*, pages 217-222, Beijing, China, July 2016.

[65] J. C. Long, Z. Y. Gao, H. L. Ren, and A. P. Lian. Urban traffic congestion propagation and bottleneck identification. *Science in China Series F: Information Sciences*, 51(7):948-964, 2008.

[66] T. Ezaki, R. Nishi, and K. Nishinari. Taming macroscopic jamming in transportation networks. *Journal of Statistical Mechanics: Theory and Experiment*, 2015(6):P06013, 2015.

[67] N. Yoshioka, T. Shimada, and N. Ito. Macroscopic fundamental diagram in simple model of urban traffic. *Artificial Life and Robotics*, 22(2):217-221, 2016.

[68] S. Lammer and D. Helbing. Self-control of traffic lights and vehicle flows in urban road networks. *Journal of Statistical Mechanics: Theory and Experiment*, 2008(04):P04019, 2008.

[69] E. Hall. The hidden dimension. *Doubleday*, NewYork, 1966.

[70] D. Katz. Animals and men. *Longmans*, Green, NewYork, 1937.

[71] D. Helbing, P. Molnar, I. J. Farkas, and K. Bolay. Self-organizing pedestrian movement. *Environment and planning B: planning and design*, 28(3):361-383, 2001.

[72] G. E. P. Box and M. E. Muller. A note on the generation of random normal deviates. *The annals of mathematical statistics*, 29(2):610-611, 1958.

bibitemBellmanR. Bellman. On the theory of dynamic programming. *Proceedings of the National Academy of Sciences*, 38(8):716-719, 1952.

[73] L. F. Henderson. On the fluid mechanics of human crowd motion. *Transportation research*, 8(6):509-515, 1974.

[74] J. R . Welty, C. E. Wicks, G. Rorrer, and R. E. Wilson. Fundamentals of momentum, heat, and mass transfer. John Wiley & Sons, 2009.

[75] K. L. Cooke and E. Halsey. The shortest route through a network with time-dependent internodal transit times. *Journal of mathematical analysis and applications*, 14(3):493-498, 1966.

[76] A. Z. Ziliaskopoulos and H. S. Mahmassani. Time-dependent, shortest-path algorithm for real-time intelligent vehicle highway system applications. *Transportation Research Record*, 1408:94-104, 1993.

[77] B. Ding, J. X. Yu, and L. Qin. Finding time-dependent shortest paths over large graphs. *Proceedings of the 11th international conference on Extending database technology: Advances in database technology*, pages 205-216, Nantes, France, March 2008.

[78] U. Demiryurek, F. Banaei-Kashani, C. Shajabi, and A. Ranganathan. Online computation of fastest path in time-dependent spatial networks. *Proceedings of International Symposium on Spatial and Temporal Databases*, pages 92-111, Minneapolis, MN, USA, August 2011.

[79] Y. Sun, X. Yu, R. Bie, and H. Song. Discovering time-dependent shortest path on traffic graph for drivers towards green driving. *Journal of Network and Computer Applications*, 83:204-212, 2017.

[80] D. Zhang, C. Y. Chow, A. Liu, X. Zhang, Q. Ding, and Q. Li. Efficient evaluation of shortest travel-time path queries through spatial mashups. *GeoInformatica*, 1-26, 2017.